

THE LOW-Z INTERGALACTIC MEDIUM. III. H I AND METAL ABSORBERS AT $Z < 0.4$

CHARLES W. DANFORTH AND J. MICHAEL SHULL

CASA, Department of Astrophysical and Planetary Sciences, University of Colorado, 389-UCB, Boulder, CO 80309;
 danforth@casa.colorado.edu, mshull@casa.colorado.edu

Draft version April 4, 2008

ABSTRACT

We conduct an ultraviolet (*HST* and *FUSE*) spectroscopic survey of H I (Lyman lines) and seven metal ions (O VI, N V, C IV, C III, Si IV, Si III, Fe III) in the low-redshift intergalactic medium (IGM) at $z < 0.4$. We analyzed 650 Ly α absorbers over redshift pathlength $\Delta z = 5.27$, detecting numerous absorbers: 83 O VI systems, 39 C III, 53 Si III, 24 C IV, 24 N V, and so on. Our survey yields distributions in column density and estimates of the IGM baryon content and metallicities of C, N, O in the IGM. In the low- z IGM, we have accounted for $\sim 40\%$ of the baryons: 30% in the photoionized Ly α forest and 10% in the ($T = 10^{5-6}$ K) warm-hot intergalactic medium (WHIM) traced by O VI. Statistical metallicities of C, N, O ions are consistent with the canonical ($z = 0$) value of 10% solar, with considerable scatter. Improved statistics for weak O VI absorbers allows us to estimate $\Omega_{\text{WHIM}}/\Omega_b = 0.073 \pm 0.008$ down to $\log N_{\text{OVI}} = 13.4$ and 0.086 ± 0.008 down to $\log N_{\text{OVI}} = 13.0$. The O VI absorber line frequency, $dN/dz = 40^{+14}_{-8}$, down to 10 mÅ equivalent width suggests a 250-300 kpc extent of metals around dwarf galaxies ($M_V = -17$ to -18). Many absorbers appear to contain multiphase gas, with both collisional ionization and photoionization determining the ionization state. N V absorption is well-correlated with O VI and both ions show similarly steep power-law indices $dN/dz \propto N^{-\beta}$ with $\beta_{\text{OVI}} \approx \beta_{\text{NV}} \approx 2$ while $\beta_{\text{HI}} = 1.7$. We conclude that O VI and N V are reliable tracers of the portion of the WHIM at $T \approx 10^{5-6}$ K. C IV may be present in both collisional and photoionized phases; N_{CIV} correlates poorly with both N_{HI} and N_{OVI} and $\beta_{\text{HI}} < \beta_{\text{CIV}} < \beta_{\text{OVI}}$. The ions C III, Si III, and Si IV are well correlated with H I and show patterns typical of photoionization. We detect Fe III in 14 absorbers with column densities higher than expected, $[\text{Fe III}/\text{Si III}] \approx 0.5 \pm 0.3$. Adjacent ion stages of the same element (C III/IV and Si III/IV) provide useful constraints on the photoionization parameter, $\log U \approx -1.5 \pm 0.5$. Comparison of Si IV and C IV with high- z surveys shows a modest increase in line density, consistent with increasing IGM metallicity at recent epochs.

Subject headings: cosmological parameters—cosmology: observations—intergalactic medium—quasars: absorption lines—ultraviolet: general

1. INTRODUCTION

We continue our far-ultraviolet (FUV) surveys of the baryon content and metallicity of the low-redshift intergalactic medium (IGM) by analyzing 650 Ly α absorbers, the largest database to date from the *Space Telescope Imaging Spectrograph* (STIS) aboard the *Hubble Space Telescope* (*HST*) and the *Far Ultraviolet Spectroscopic Explorer* (*FUSE*). These spectrographs offer sensitive probes of H I (Lyman lines) together with associated metal-line absorbers. Of particular importance are UV absorption lines from high ion stages (O VI, N V) produced primarily in hot, collisionally ionized gas, as well as lower ion stages (C IV, C III, Si IV, Si III, Fe III) that can arise in both photoionized gas and hot gas. The advent of these sensitive FUV spectrographs has stimulated an increase in our understanding of the low-redshift IGM.

In this survey, we address several astronomical questions facilitated by a more accurate census of baryons and heavy elements in the IGM. From observations with *HST*, *FUSE*, and *Chandra*, it seems likely (Shull 2003; Stocke et al. 2006a; Nicastro et al. 2005) that most of the baryons still reside in the IGM, even at low redshift. But in what thermal phase and ionization state do they exist, and with what spatial distribution? What are the physical properties (temperature, density) of the low- z absorbers? From their metallicities and nucleosynthetic patterns, can we uncover their stellar sources? By

comparing the spatial proximity of metal-line absorbers to neighboring galaxies, can we estimate the extent of metal transport into the IGM? In this paper, we attempt to make progress on all of these issues.

Over the past decade, the Colorado group and others (e.g., Tripp et al. 2008) have focused on UV studies of H I and O VI absorbers in the low- z IGM (Penton, Stocke, & Shull 2000, 2004; Tripp, Savage, & Jenkins 2000; Savage et al. 2002). Danforth & Shull (2005) and Danforth et al. (2006), hereafter denoted Papers 1 and 2, respectively, analyzed IGM absorption at $z \leq 0.3$ in *FUSE* sight lines toward 31 AGN with high-quality data from STIS and *FUSE*. Those studies began with a set of 171 strong Ly α absorbers (equivalent widths $W_\lambda \geq 80$ mÅ) taken from the literature (Penton, Stocke, & Shull 2000, 2004, and other sources). Because Ly α lines are subject to instrumental broadening and line saturation, we endeavored to measure higher-order Lyman transitions (Ly β –Ly η) in the *FUSE* data at $z_{\text{abs}} < 0.3$ in order to obtain accurate curve-of-growth (CoG) solutions to the doppler parameter, b_{HI} , and neutral hydrogen column density, N_{HI} . As first noted in *FUSE* studies of Ly β /Ly α (Shull et al. 2000) and confirmed in Paper 2, the Ly α measurements alone will systematically underestimate N_{HI} , a discrepancy that increases in stronger lines, and overestimate b_{HI} . Paper 2 also confirmed the result of Penton, Stocke, & Shull

(2004) that the column-density distribution of H I absorbers follows a power law, $dN/dN_{\text{HI}} \propto N_{\text{HI}}^{-\beta}$, with $\beta_{\text{HI}} = 1.68 \pm 0.11$. The CoG-derived b -values show that most of the H I absorbers arise in gas with $T < 10^5$ K, incompatible with their existence in a hot (shock-heated) IGM phase. A small population of broad, shallow Ly α absorbers may probe trace amounts of H I in hot, highly ionized gas (Richter et al. 2004; Lehner et al. 2007).

Along with the H I lines, Papers 1 and 2 measured corresponding absorption lines of the metal ions O VI $\lambda\lambda 1031.926, 1037.617$ and C III $\lambda 977.020$. We found O VI to be the most accessible tracer of the warm-hot ionized medium (WHIM), thought to arise in shock-heated gas at $T = 10^{5-6}$ K (Davé et al. 1999; Cen & Ostriker 1999). The FUV lines of O VI are currently the best tracer of the “cooler” portions of these shocks, reaching a peak ionization fraction, $f_{\text{OVI}} \approx 0.22$ at temperature $T_{\text{max}} = 10^{5.45}$ K in collisional ionization equilibrium or CIE (Sutherland & Dopita 1993) and similar values in non-equilibrium cooling (Gnat & Sternberg 2007). Owing to the relatively high solar oxygen abundance, $(\text{O}/\text{H})_{\odot} \approx 5 \times 10^{-4}$, and the substantial oscillator strength of the stronger line of the O VI doublet (1031.9261 Å, $f = 0.1325$), the O VI ultraviolet transitions are detectable down to column densities $N_{\text{OVI}} \approx 10^{13} \text{ cm}^{-2}$, more than two orders of magnitude below the current sensitivity of the X-ray absorption lines of O VII (21.602 Å, $f = 0.696$) and O VIII (18.969 Å, $f = 0.416$) studied with *Chandra* and *XMM-Newton*. Although the ($1s-2p$) X-ray transitions are crucial for detecting the hotter WHIM at $T > 10^6$ K, their intrinsic line strengths, $f\lambda$, are much weaker than the ($2s-2p$) O VI ultraviolet transitions and the detection limits and velocity resolution of current X-ray instruments make them much less sensitive.

Papers 1 and 2 represented a significant statistical improvement over previous studies of small numbers of sight lines (e.g. Tripp, Savage, & Jenkins 2000; Savage et al. 2002) with 40 O VI detections and $\Delta z \approx 2.2$ vs. approximately 10 O VI absorbers over $\Delta z \sim 0.5$. The detection statistics were sufficient for us to draw a number of intriguing conclusions. We found that N_{OVI} was poorly correlated with N_{HI} , and the power-law distribution of O VI column density, $\beta_{\text{OVI}} = 2.2 \pm 0.1$, was significantly steeper than for H I. These results implied a multiphase IGM with hot, shocked WHIM (traced by O VI) kinematically associated with cooler, photoionized H I. We inferred a total cosmological mass fraction in the WHIM of at least $\Omega_{\text{WHIM}} = (0.0022 \pm 0.0003) [h_{70} (Z_{\odot}/0.1Z_{\odot}) (f_{\text{OVI}}/0.2)]^{-1}$ or $4.8 \pm 0.9\%$ of the total baryonic mass at $z < 0.15$. Unlike O VI, the 30 C III detections showed reasonable column density correlation with H I, and the dN/dz distributions showed similar slopes, suggesting that C III is predominantly photoionized.

In this survey (Paper 3), we expand the parameter space of the low- z IGM survey, using a much larger data set of 650 Ly α absorbers, observed over a total redshift pathlength $\Delta z = 5.27$ (compared to $\Delta z = 2.2$ in Papers 1 and 2). There were several limitations inherent in our initial survey. Our combined STIS/E140M+*FUSE* spectral survey provides an expansion and improvement in three important ways:

(1) In Paper 1, we limited our search to “strong” Ly α systems ($W_{\text{Ly}\alpha} > 80 \text{ mÅ}$). However, Penton, Stocke, & Shull (2004) showed that the median $W_{\text{Ly}\alpha} = 68 \text{ mÅ}$, so this equivalent-width threshold eliminated more than half of the possible IGM systems from study. Furthermore, Paper 1 found little if any correlation between N_{HI} and N_{OVI} . Indeed, at low column densities, $\log N_{\text{HI}} \leq 13.4$, we found many absorbers with $N_{\text{OVI}} \approx N_{\text{HI}}$. Thus, measurable O VI absorption is possible even in weak H I absorbers. We relax this “Ly α bias” here by measuring metal ion absorption in all detected Ly α systems.

(2) The combined STIS/E140M+*FUSE* dataset covers a large wavelength range: 905–1710 Å in all cases and out to 1729 Å in most of the datasets. We use the longer wavelengths available in the E140M data to measure H I, O VI, and C III at higher redshifts than were possible in the *FUSE* data alone ($z_{\text{OVI}} \leq 0.15$). We now cover Ly α out to $z \leq 0.4$ and measure higher-order Lyman lines in strong systems to even higher redshifts in some sight lines. This expanded redshift space more than doubles the O VI absorber pathlength.

(3) We use the broad spectral coverage of STIS to measure metal ions not found in *FUSE* data. Lines of N V and C IV can exist at temperatures nearly as high as O VI, and they may provide additional tracers of the cooler WHIM. We also measure lines of Si IV, Si III, and Fe III, which trace predominantly photoionized material. By observing adjacent ionization states of the same elements (C III/IV, Si III/IV), we can make direct ionization measurements without the complication of relative abundance uncertainties.

In § 2, we discuss our selection of AGN sight lines and the rationale behind our choice of spectral lines. In § 2.2 and § 2.3, we discuss our technique for Ly α line identification and the measurement and verification of metal ion lines. In § 2.4 and § 2.5, we detail our analytic procedure and methods for deriving quantities of cosmological interest such as dN/dz , β_{ion} , metallicity, and Ω_{ion} . Our basic detection results are presented in § 3.1. We compare new H I, O VI, and C III results to those of previous work and discuss the new ions (C IV, N V, Si III, Si IV, Fe III) in this context. In § 3.2, we compare observed line ratios with a set of CLOUDY models to derive typical IGM ionization parameters and temperatures. We discuss the implications of these results to cosmology in § 3.3. In § 4 we summarize our conclusions.

2. OBSERVATIONS AND DATA ANALYSIS

2.1. Sight Line Selection and Data Reduction

We have performed detailed *FUSE*+STIS analyses on sight lines toward 35 bright AGN. The primary objective of this census is to remove as much “rich sight line” bias as possible, while accumulating the longest available pathlength through the low-redshift IGM. Therefore, we included *all* available AGN with both *FUSE* and STIS/E140M data of reasonable quality. The combined dataset covers 905–1710 Å at a resolution of 20 km s^{-1} or better, at a signal to noise per resolution element $(S/N)_{\text{res}} \gtrsim 5$ in most cases. This gives us a potential redshift pathlength out to $z \gtrsim 0.4$ in Ly α , Ly β , O VI, C III, and most of the other species, but only out to $z \approx 0.1$ in C IV. Five of our sight lines (3C 273, Akn 654,

TABLE 1
FUSE+STIS IGM SIGHT LINES

Sight Line	R.A. (J2000.0)	Decl. (J2000.0)	z_{AGN}	STIS (ksec)	FUSE (ksec)	Unid. Papers I & II ^a
Mrk 335	00 06 19.5	+20 12 10	0.025785	17.1	97.0	Y
HE 0226–4410	02 28 15.2	–40 57 16	0.495	43.8	33.2	Y
PKS 0312–770	03 11 55.2	–76 51 51	0.223000	8.4	5.5	N
PKS 0405–123	04 07 48.4	–12 11 37	0.572590	27.2	71.1	N
HS 0624+6907	06 30 02.5	+69 05 04	0.370000	62.0	112.3	Y
PG 0953+414	09 56 52.4	+41 15 22	0.234100	8.0	72.1	Y
Ton 28	10 04 02.5	+28 55 35	0.329700	33.0	11.2	Y
3C 249.1	11 04 13.7	+76 58 58	0.311500	68.8	216.8	N
PG 1116+215	11 19 08.6	+21 19 18	0.176500	26.5	77.0	Y
PG 1211+143	12 14 17.7	+14 03 13	0.080900	42.5	52.3	Y
PG 1216+069	12 19 20.9	+06 38 38	0.331300	5.8	12.0	N
Mrk 205	12 21 44.0	+75 18 38	0.070846	62.1	203.6	N
3C 273	12 29 06.7	+02 03 09	0.158339	18.7	42.3	N
Q 1230+0115	12 30 50.0	+01 15 23	0.117000	9.8	4.0	N
PG 1259+593	13 01 12.9	+59 02 07	0.477800	95.8	668.3	Y
PKS 1302–102	13 05 33.0	–10 33 19	0.278400	4.8	142.7	Y
Mrk 279	13 53 03.4	+69 18 30	0.030451	54.6	228.5	Y
NGC 5548	14 17 59.5	+25 08 12	0.017175	69.8	55.0	Y
Mrk 1383	14 29 06.6	+01 17 06	0.086470	10.5	63.5	Y
PG 1444+407	14 46 45.9	+40 35 06	0.267300	48.6	10.0	N
Mrk 876	16 13 57.2	+65 43 10	0.129000	29.2	46.0	N
3C 351	17 04 41.4	+60 44 31	0.371940	77.0	141.9	Y
H 1821+643	18 21 57.3	+64 20 36	0.297000	50.9	132.3	Y
Mrk 509	20 44 09.7	–10 43 25	0.034397	7.6	62.3	Y
PHL 1811	21 55 01.5	–09 22 25	0.190000	33.9	75.0	Y
PKS 2155–304	21 58 52.0	–30 13 32	0.116000	10.8	123.2	Y
Akn 564	22 42 39.3	+29 43 31	0.024684	10.3	60.9	Y
NGC 7469	23 03 15.6	+08 52 26	0.016317	22.8	44.3	Y

^a Sight line included in Papers I & II?

Mrk 509, Mrk 205, and PG 1116+215) are lacking the longest wavelength order of the STIS echelle data and truncate at $\lambda = 1709$ Å. The other 30 sight lines include the zeroth-order data at $1711 < \lambda < 1729$ Å, which we include where possible.

Of the 35 sight lines, we excluded six targets (NGC 3516, NGC 3783, NGC 4051, NGC 4151, NGC 4395, and NGC 4593) at $z_{\text{AGN}} \leq 0.01$ because the available redshift pathlength is minimal and any absorbers could be intrinsic to either our Galaxy or the AGN. We also excluded the high-redshift object HS 1700+6416 ($z = 2.72$) since its interpretation was greatly complicated by high- z EUV lines from several partial Lyman-limit systems (Fechner et al. 2006). Our final sample of 28 AGN sight lines is presented in Table 1. They cover a total Ly α redshift pathlength of $\Delta z = 5.27$ with $\langle z_{\text{Ly}\alpha} \rangle \approx 0.14$ and $\langle z_{\text{AGN}} \rangle = 0.21$.

We retrieved the FUSE data from the Multimission Archive at the Space Telescope Science Institute (MAST) archive and reduced them as in Paper 2. We binned the data by three instrumental pixels. The FUSE instrumental resolution of ~ 20 km s^{–1} typically represents 8–10 pixels or ~ 3 bins. We used primarily FUSE data from the highest-throughput LiF1 channel (Moos et al. 2000), but went to LiF2 or SiC channels when LiF1 did not cover the region of interest or to provide a check on marginal LiF1 detections. The archival STIS/E140M data were reduced at the University of Colorado by S. V. Penton. We smoothed the data over three pixels to better match the nominal instrumental resolution of ~ 7 km s^{–1}. Data from both instruments were normalized in overlapping 10 Å segments. We selected line-free continuum regions interactively and fitted the spectral continuum using low-

order Legendre polynomials. For each 10 Å segment, we calculated the local S/N from the standard deviation of the normalized continuum data about the fitted contin-

2.2. Identification of Ly α Absorbers

We identified the associated higher Lyman lines and metal absorption systems using the Ly α lines as “signposts”. In the software, we displayed the normalized STIS/E140M spectrum in 10 Å segments, marking the ISM lines and IGM line positions corresponding to previously-identified Ly α systems (e.g., Figures 1 and 2). Any unidentified line was centroided, measured, and initially assumed to be Ly α . For weak lines, including broad shallow absorbers, we expect the optical depths to be in the ratio, $\tau(\text{Ly}\alpha)/\tau(\text{Ly}\beta) \approx 6.2$. If the wavelength and equivalent width at the position of the corresponding Ly β and higher-order Lyman lines were consistent with the Ly α identification, we accepted the absorber and entered it into a database. For strong absorbers ($W_{\text{Ly}\alpha} \gtrsim 150$ mÅ), we would expect to detect Ly β or higher-order Lyman lines. Quite a few potential strong lines, initially assumed to be Ly α , were ruled out by this criterion. Line identification was an iterative process: we assumed weak, unidentified lines to be Ly α until proven otherwise. More careful analysis occasionally showed that lines identified as weak Ly α were better explained as metal lines of stronger IGM systems, high-order Lyman lines of a strong higher-redshift system, intrinsic AGN features, high velocity components of Galactic lines, or instrumental artifacts.

Since the rest-frame line density of FUV absorbers increases dramatically at shorter wavelengths, we began our Ly α search at long wavelengths and worked our way to the blue. The identification process was carried out iteratively until all absorption features were either identified or ruled out as not being Ly α systems. In several cases, Ly α lines were blended or redshifted beyond the long wavelength end of the data (1710 or 1729 Å, $z_{\text{abs}} > 0.406$ or 0.422, depending on sight line), and strong H I absorbers were then identified through their Ly β absorption. Our Ly α identifications were informed by those of previous work, in particular Penton, Stocke, & Shull (2000, 2004), but we searched each sight line and verified each absorber independently.

Although some fraction of strong IGM systems are composed of multiple velocity components, this is not always apparent in the often-saturated Ly α line profiles. In cases where higher Lyman lines showed multiple, unambiguously separable components in Ly α or Ly β , we treated each component as a separate absorber. However, most profiles were consistent with single components or showed some asymmetry which we could not split unambiguously into multiple features. These cases (the majority) are treated as single absorbers. Our counting statistics are intermediate between the “component” and “system” nomenclature of Tripp et al. (2008), but generally closer to the latter classification.

In total, we identified 660 H I absorbers via Ly α and/or Ly β absorption and found several discrepancies with published line lists. We truncated the line list at $z = 0.4$ since data quality falls rapidly beyond 1700 Å.

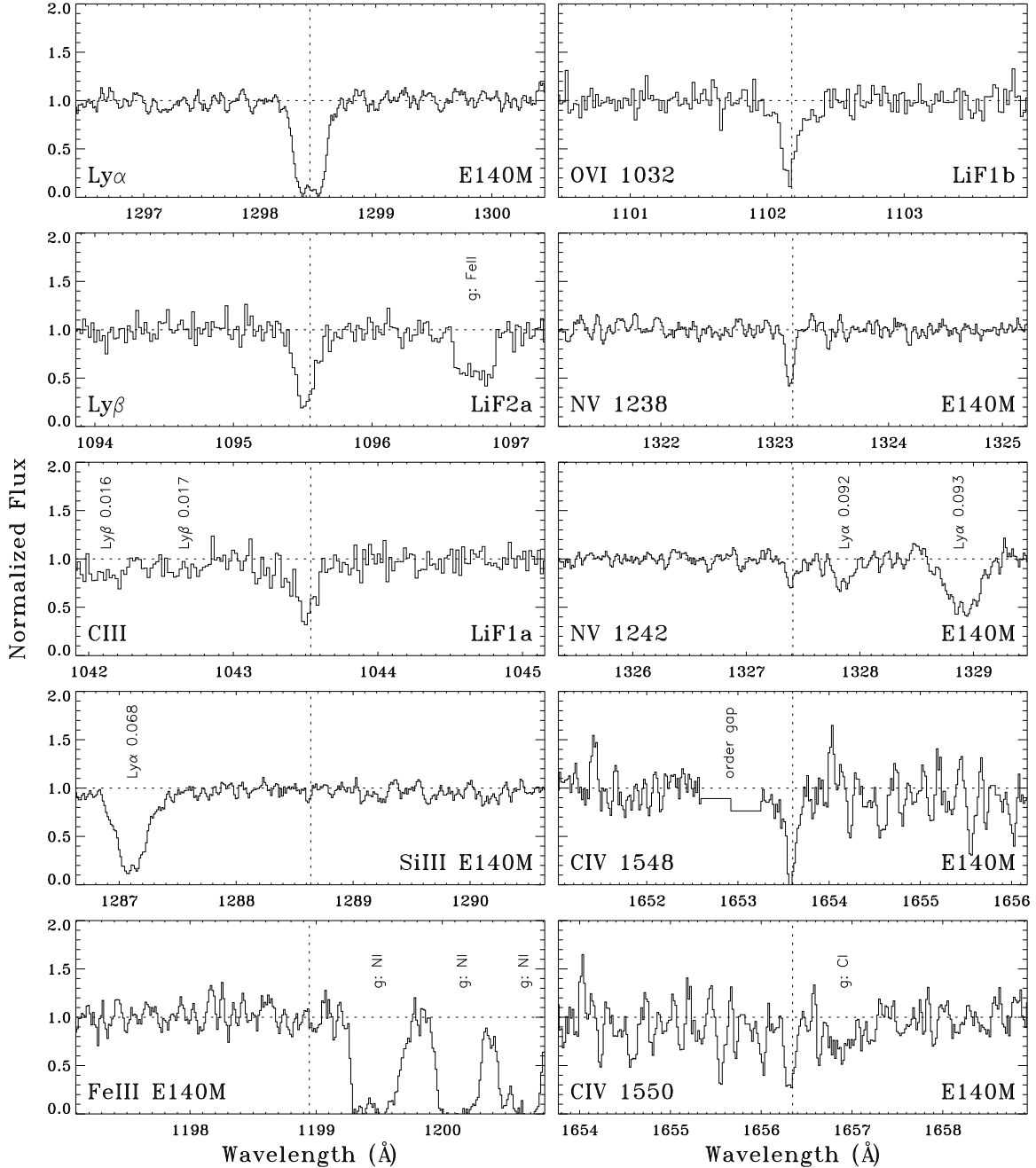


FIG. 1.— IGM absorption in the $z = 0.06808$ absorber toward PG 0953+414 showing typical, normalized *FUSE* and STIS/E140M data. $\text{Ly}\alpha$ and $\text{Ly}\beta$ (top left) show strong, consistent profiles ($W_{\text{Ly}\alpha} = 284 \pm 13 \text{ m}\text{\AA}$ and $W_{\text{Ly}\beta} = 128 \pm 16 \text{ m}\text{\AA}$). CIII is detected but SiIII and FeIII are non-detections. High ions are depicted in the right hand panels: OVI $\lambda 1032$ and both NV lines (center left) are detected with consistent profiles. The OVI $\lambda 1038$ line is blended with a strong H_2 transition and is not shown. CIV shows noisy but consistent detections in both bands of the doublet as well. The two SiIV transitions are not shown. Each panel is centered at the redshifted wavelength of the transition and covers $\pm 500 \text{ km s}^{-1}$ in either direction. Other detected features in the data are identified. The “g:” prefix denotes a Galactic absorption line, while a numerical suffix denotes the redshift of an IGM line. The source channel (e.g. STIS/E140M or *FUSE* LiF2a) is indicated in the lower right.

This left us with a total of 650 IGM systems, presented¹ in Table 2.

2.3. Line Measurements and Consistency Checks

The next step was to perform detailed measurements of 11 UV resonance absorption transitions of seven ion

¹ Truncated sample tables are presented here. Full versions can be seen in the electronic version.

species (Table 3), spanning a range of ionization levels and strengths. In particular, O VI and C IV are normally interpreted as tracers of hot gas, with peak ionization fractions (f_{ion}) at temperature T_{max} in collisional ionization equilibrium (CIE). As computed by Sutherland & Dopita (1993), O VI has maximum CIE abundance of $f_{\text{OVI}} = 0.22$ at $\log T_{\text{max}} = 5.45$, N V reaches $f_{\text{NV}} = 0.24$ at $\log T_{\text{max}} = 5.25$, and $f_{\text{CIV}} =$

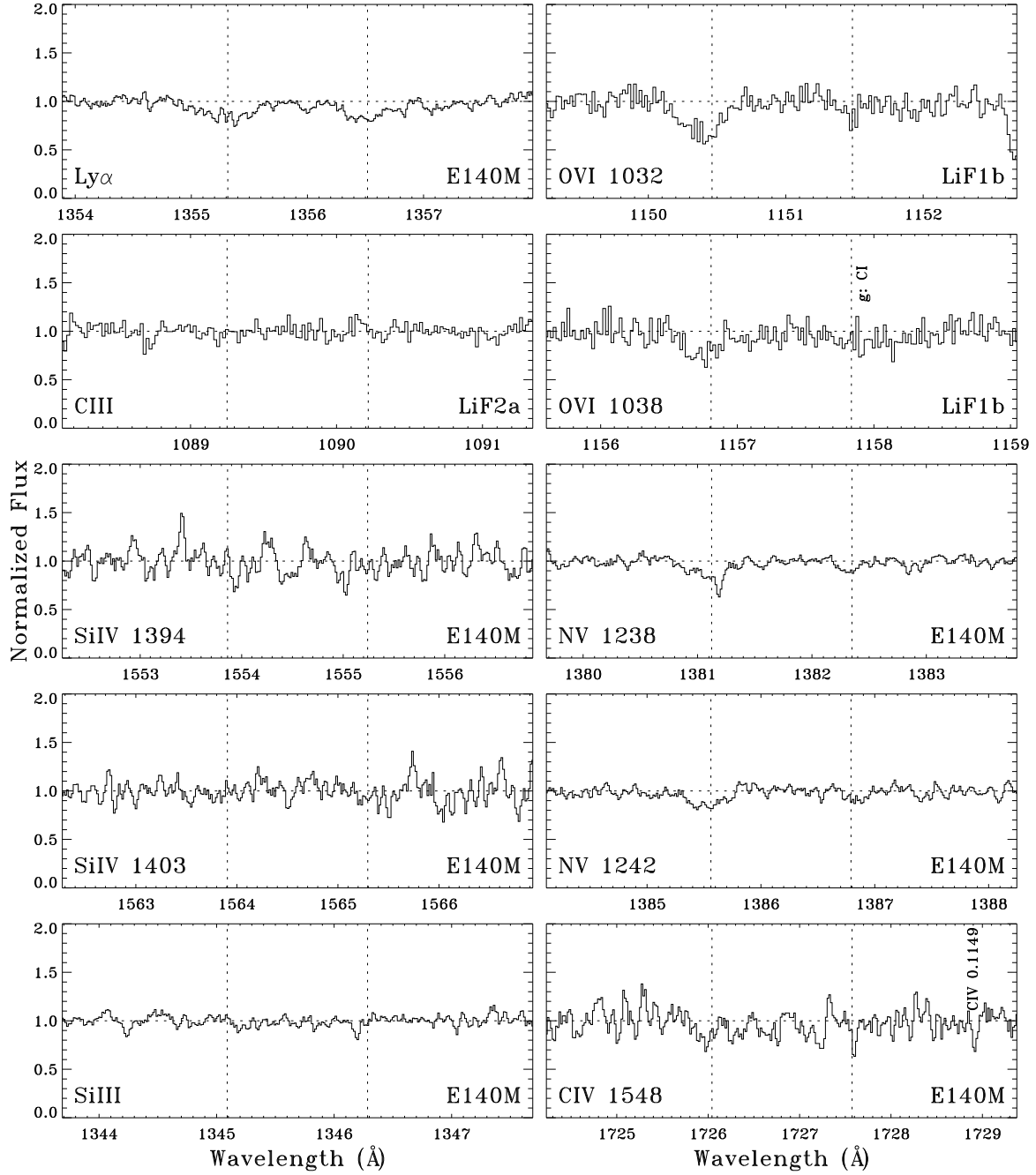


FIG. 2.— Same as Fig. 1 for two absorbers in the Mrk876 sight line. The vertical dashed lines in the panels show the redshifted locations of the $z = 0.11487$ (left) and $z = 0.11586$ (right) absorbers. Both absorbers show weak, broad $\text{Ly}\alpha$ profiles ($W_{\text{Ly}\alpha} = 87 \pm 13$ and 74 ± 5 mÅ, respectively), and the expected $\text{Ly}\beta$ equivalent widths are below the level of the noise and are not shown. CIII shows a clean non-detection at both redshifts. Data from the stronger SiIV transition ($\lambda 1394$) is consistent with noise and a better upper limit is given by the weaker SiIV $\lambda 1403$ line. SiIII shows a clean non-detection at $z = 0.11487$, but a marginal detection at $z = 0.11586$. The Li-like ions are a different matter: OVI and NV absorption is detected at both redshifts in both lines of both ions (OVI $\lambda 1038$ line at $z = 0.11586$ is blended with a weak Galactic CI line and is taken as an upper limit). Both systems show weak CIV 1548Å detections. CIV 1550Å is detected for $z = 0.11487$, but is redshifted out of the data range for $z = 0.11586$.

TABLE 2
SAMPLE HI ABSORBERS

Sight Line	z_{abs}	$W_r(\text{Ly}\alpha)$ (mÅ)	$W_r(\text{Ly}\beta)$ (mÅ)	$W_r(\text{Ly}\gamma)$ (mÅ)	$W_r(\text{Ly}\delta)$ (mÅ)	b_{HI} (km s ⁻¹)	$\log N_{\text{HI}}$ (N in cm ⁻²)	method ^a
Mrk 335	0.00653	210 ± 19	59 ± 8	20 ⁺⁷ ₋₄	13.99 ^{+0.10} _{-0.11}	COG
Mrk 335	0.00759	78 ± 3	< 13	33 ± 4	13.24 ^{+0.06} _{-0.05}	Lyα AOD
Mrk 335	0.02086	149 ± 4	42 ± 7	< 205	< 29	60 ± 2	13.51 ± 0.02	Lyα AOD
HE 0226-4410	0.01216	50 ± 3	< 18	41 ± 7	13.06 ^{+0.08} _{-0.07}	Lyα AOD
HE 0226-4410	0.02682	66 ± 10	23 ± 4	30 ± 4	13.17 ^{+0.12} _{-0.05}	Lyα AOD
HE 0226-4410	0.02729	30 ± 5	< 18	31 ± 5	12.79 ^{+0.13} _{-0.09}	Lyα AOD
HE 0226-4410	0.04129	40 ± 4	< 19	32 ± 7	12.93 ^{+0.09} _{-0.07}	Lyα AOD
HE 0226-4410	0.04609	157 ± 12	41 ± 3	16 ⁺⁴ ₋₃	13.84 ^{+0.06} _{-0.09}	COG
HE 0226-4410	0.05177	26 ± 3	< 26	~ 17	12.76 ^{+0.27} _{-0.12}	Lyα AOD
HE 0226-4410	0.05814	30 ± 10	...	< 14	< 29	12 ± 3	12.77 ± 0.14	Lyα fit

^a HI solution method: AOD=integrated apparent optical depth, fit=Voigt fit, COG=multi-line curve of growth solution, COG[†]=poorly-constrained curve of growth.

TABLE 3
IGM DIAGNOSTIC LINES

ion	λ_{rest} (Å)	f ^a	$[X/H]_{\odot}$ ^b	I.P. ^c (eV)	$f_{\text{ion,CIE}}$ ^c	$\log T_{\text{max}}$
HI	1215.67	0.4164	0.00	<13.6	...	<4.19 ^d
	1025.72	0.07914				
Fe III	1122.52	0.0544	-4.55	16-31	0.89	4.27-4.58 ^d
Si III	1206.50	1.63	-4.49	16-35	0.90	4.30-4.85 ^d
C III	977.02	0.757	-3.61	24-48	0.83	4.66-5.01 ^d
Si IV	1393.76	0.514	-4.49	35-48	0.35	4.8 ^e
	1402.70	0.255				
C IV	1548.20	0.191	-3.61	48-65	0.29	5.0 ^e
	1550.77	0.095				
N V	1238.82	0.157	-4.22	78-98	0.24	5.25 ^e
	1242.80	0.078				
O VI	1031.93	0.1325	-3.34	114-138	0.22	5.45 ^e
	1037.62	0.0658				

^a Line oscillator strength (Morton 2003) ^b Solar photospheric element abundance $\log(X/H)$; Asplund et al. (2005) ^c Peak ion fraction under CIE via Sutherland & Dopita (1993); value used in Ω_{ion} and Z_{ion} calculations over the listed range in ionization potential. ^d Temperature range over which ion is dominant under collisional ionization equilibrium, via Sutherland & Dopita (1993) ^e Ion is never dominant under CIE. Listed temperature is peak CIE abundance.

0.29 at $\log T_{\max} = 5.00$. Non-equilibrium ionization effects may alter the post-shock ionization fractions (Rajan & Shull 2008). Because N V lies intermediate in ionization potential between the two other Li-like ions, it should be a good WHIM tracer as well. However, the solar nitrogen abundance is more than five times lower than oxygen, and nitrogen is often observed to be underabundant in Galactic HVCs (Gibson et al. 2001; Collins et al. 2003). Until now, N V absorption is largely an unknown quantity in the low- z IGM.

The UV lines of Si IV $\lambda\lambda 1393.755, 1402.770$, Si III $\lambda 1206.500$, C III $\lambda 977.020$, and Fe III $\lambda 1122.526$ are all strong transitions of abundant metals, with production ionization potentials below 3 ryd (40.8 eV) and expected to probe photoionized, metal-enriched material. In these lines, we also have two sets of adjacent ionization levels (C III/IV and Si III/IV), which may help to define the ionization state of the absorbers, independent of elemental abundance ratios. Highly ionized metals were the primary focus of this survey and singly-ionized species were not explicitly studied. However, low-ion absorption exists in some Ly α IGM systems (Tripp et al. 2008) and in many ionized HVCs (Sembach et al. 1999; Collins et al. 2003, 2007). In a future paper, we will examine the behavior of Si II, C II, Fe II, and similar species in the IGM and give further analysis options in adjacent ionization stages (Si II/III/IV, C II/III/IV, Fe II/III).

We examined all 13 transitions for each IGM absorber; Figures 1 and 2 show examples. In each case, we measured the line using the apparent optical depth (AOD) method (Sembach & Savage 1992) and/or fitted the line with a Voigt profile (see discussion in Paper 2 and sources therein). While the Voigt and AOD methods generate equivalent line measurements and uncertainties in most cases, each has its advantages; AOD is preferable for weak, asymmetric, or noisy lines, while Voigt fits are more reliable for saturated or blended lines. In cases where no line was apparent, we measured a 4σ upper limit on equivalent width, W_λ , according to

$$W_{\min} = \frac{4 \lambda}{R (S/N)_\lambda}, \quad (1)$$

where we adopted instrumental resolutions, $R = \lambda/\Delta\lambda$, for the two spectrographs of $R_{\text{FUSE}} = 15,000$ and $R_{\text{STIS/E140M}} = 42,000$. In cases where the measured $W_\lambda \leq W_{\min}$, we declared the line to be an upper limit. Heavily blended lines, in which no information was available, and lines that were redshifted out of the data range were noted but ignored. Measurements of less severely blended lines and lines with ambiguous identification were measured and taken to be upper limits.

In the second stage of processing, we checked our detections for consistency. We required the Ly β detections or upper limits to be consistent with Ly α measurements, and the metal doublets (C IV, N V, O VI, Si IV) to be consistent within the error bars in $\log N$. The singlet lines (C III, Si III, Fe III) were harder to verify this way, but we were able to confirm or rule out many based on detections or non-detections in similar ions in the same absorption system.

We carried out a third-stage vetting process of all metal-line detections to eliminate likely fixed pattern detector noise (Sahnow et al. 2000) masquerading as weak detections, instrumental artifacts, and other inconsisten-

cies. In some cases a “detection” was indistinguishable from adjacent data fluctuations and there was no other supporting evidence such as detections in other ions in the same absorber. Such cases were deemed suspect and demoted to upper limits even though they were technically $> 4\sigma$. The effects of this process on the detection statistics varied. Unfortunately, an unknown number of weak but bona-fide detections may have been eliminated in this check, but the remaining detections are much more robust than in the earlier stages. The elimination of some marginal detections is apparent in the low- N turn-overs seen in some dN/dz plots (see below for discussion). If we assume that absorbers follow a power-law distribution with N , we can assess the effect of this final detection verification step. However, the low- N distribution of metal-line absorbers may also be truncated owing to the limited volumes over which galaxies can disperse metals (Tumlinson & Fang 2005, Paper 1).

The final processing stage involved deriving column densities and b -values for the different species. We determined most (69%) of the H I values directly from Ly α measurements. Paper 2 showed that Ly α -only measurements underestimate N_{HI} , owing to saturation and the lack of CoG information from higher Lyman lines. The effect is strongest in saturated lines and is probably negligible for $W_{\text{Ly}\alpha} \lesssim 100$ mÅ. The median equivalent width in our sample is $W_{\text{Ly}\alpha} = 94$ mÅ. Eleven H I absorbers were measured from Ly β only, when Ly α was strongly blended or redshifted out of the E140M spectral range ($z \gtrsim 0.4$). Values of column density and doppler width for strong H I absorbers were usually (30%) determined from concordance CoG plots (see Paper 2 for discussion). In some cases, we measured Ly γ and Ly δ to further constrain the H I solution. Lyman-line equivalent widths and the derived b_{HI} and N_{HI} measurements are listed in Table 2.

We took column densities and b -values of the doublet ions (O VI, N V, C IV, Si IV) as the error-weighted mean of the two lines, when possible, or as measured if only one line was available. Values for the single lines (C III, Si III, Fe III) were taken as measured by the AOD or Voigt profile methods. We present truncated tables of the measured equivalent widths, b -values, and column densities for all seven ions in Tables 4–10. Note that AOD-measured b -values are equivalent to Voigt fit measurements for strong lines, but become increasingly uncertain for weak and noisy lines. Some of the poorly-determined b -values are listed as approximate and AOD b -values in the tables should generally be treated with caution. Full versions of the Tables, including both detections and upper limits, are available in the electronic edition.

2.4. Absorber Statistics

With such a large database of detections, we are able to analyze the absorber statistics with considerably more confidence. We constructed histograms showing the number of absorbers, \mathcal{N}_i , in logarithmic bins of width 0.2 dex in column density. In general, the median column density uncertainty, $\delta \log N$, for the metal ion detections is larger than half a bin size. We analyzed the distribution $\mathcal{N}(\log N)$ using a “distributed-power” histogram technique to spread the power of each detection across

TABLE 4
SAMPLE O VI DETECTIONS

Sight Line	z_{abs}	b (1032) (km s ⁻¹)	W_r (1032) (mÅ)	b (1038) (km s ⁻¹)	W_r (1038) (mÅ)	b (O VI) (km s ⁻¹)	$\log N(\text{O VI})$ (N in cm ⁻²)	notes
HE 0226–4410	0.20700	34 ± 1	184 ± 10	34 ± 8	111 ± 4	34 ± 8	14.33 ± 0.06	fit, AOD
HE 0226–4410	0.22004	~ 16	12 ± 1	...	< 31	~ 16	13.05 ± 0.15	AOD
HE 0226–4410	0.24515	~ 29	23 ± 1	~ 18	10 ± 1	~ 25	13.29 ± 0.15	AOD, AOD
HE 0226–4410	0.31833	6 ± 3	9 ± 2	...	< 7	6 ± 3	12.97 ± 0.17	AOD
HE 0226–4410	0.34031	21 ± 2	74 ± 11	...	< 82	21 ± 2	13.75 ± 0.05	fit
HE 0226–4410	0.35493	13 ± 9	9 ± 3	...	< 8	13 ± 9	12.94 ± 0.26	AOD
HE 0226–4410	0.35524	44 ± 6	63 ± 2	35 ± 5	22 ± 1	41 ± 6	13.69 ± 0.08	AOD, AOD
PKS 0312–770	0.20192	~ 40	31 ± 1	~ 40	13.76 ± 0.15	AOD
PKS 0312–770	0.20275	62 ± 2	527 ± 28	66 ± 2	323 ± 16	63 ± 2	14.85 ± 0.07	fit, fit
PKS 0405–123	0.09657	40 ± 20	59 ± 31	14 ± 13	32 ± 27	31 ± 20	13.71 ± 0.21	fit, fit
PKS 0405–123	0.16714	82 ± 4	470 ± 40	61 ± 5	198 ± 18	75 ± 10	14.68 ± 0.05	fit, AOD

TABLE 5
SAMPLE CIV DETECTIONS

Sight Line	z_{abs}	b (1548) (km s ⁻¹)	W_r (1548) (mÅ)	b (1550) (km s ⁻¹)	W_r (1550) (mÅ)	b (CIV) (km s ⁻¹)	$\log N(\text{CIV})$ (N in cm ⁻²)	notes
PKS 0312–770	0.10877	22 ± 1	78 ± 11	...	< 55	22 ± 1	13.52 ± 0.25	AOD
HS 0624+6907	0.06348	25 ± 1	113 ± 3	~ 27	44 ± 3	25 ± 1	13.49 ± 0.09	AOD, AOD
HS 0624+6907	0.07573	10 ± 1	45 ± 4	12 ± 3	21 ± 6	10 ± 3	13.06 ± 0.07	fit, fit
PG 0953+414	0.04960	17 ± 5	33 ± 6	...	< 22	17 ± 5	12.98 ± 0.16	AOD
PG 0953+414	0.06808	11 ± 1	135 ± 24	10 ± 1	93 ± 18	10 ± 1	13.83 ± 0.09	fit, fit
PG 1211+143	0.05104	46 ± 1	260 ± 4	33 ± 2	143 ± 2	41 ± 6	14.04 ± 0.04	AOD, AOD
PG 1211+143	0.06447	46 ± 5	73 ± 12	39 ± 6	49 ± 10	43 ± 6	13.32 ± 0.07	fit, fit
PG 1211+143	0.06493	24 ± 5	31 ± 5	~ 46	38 ± 5	24 ± 5	13.10 ± 0.21	fit, AOD
Mrk 205	0.00443	50 ± 10	362 ± 14	55 ± 2	235 ± 9	51 ± 10	14.05 ± 0.18	AOD, AOD
Mrk 205	0.02746	...	< 131	~ 17	53 ± 1	~ 17	13.55 ± 0.10	AOD
Q 1230+0115	0.04886	21 ± 9	39 ± 1	...	< 21	21 ± 9	13.00 ± 0.16	fit

TABLE 6
SAMPLE NV DETECTIONS

Sight Line	z_{abs}	b (1238) (km s ⁻¹)	W_r (1238) (mÅ)	b (1242) (km s ⁻¹)	W_r (1242) (mÅ)	b (NV) (km s ⁻¹)	$\log N(\text{NV})$ (N in cm ⁻²)	notes
PKS 0312–770	0.20192	8 ± 1	25 ± 4	9 ± 2	17 ± 3	8 ± 2	13.12 ± 0.07	fit, fit
PKS 0312–770	0.20275	67 ± 4	133 ± 10	56 ± 6	63 ± 7	63 ± 6	13.74 ± 0.04	fit, fit
PKS 0405–123	0.16714	51 ± 5	143 ± 16	...	< 155	51 ± 5	13.83 ± 0.04	fit
PKS 0405–123	0.33400	~ 12	28 ± 1	~ 12	13.52 ± 0.12	AOD
PKS 0405–123	0.36079	24 ± 8	46 ± 11	24 ± 8	13.47 ± 0.12	AOD
HS 0624+6907	0.29530	18 ± 5	30 ± 2	7 ± 3	11 ± 1	14 ± 5	13.17 ± 0.13	AOD, AOD
PG 0953+414	0.06808	8 ± 1	45 ± 4	15 ± 2	30 ± 5	10 ± 3	13.46 ± 0.05	fit, fit
PG 0953+414	0.23350	9 ± 3	11 ± 5	...	< 8	9 ± 3	12.68 ± 0.14	fit
3C 249.1	0.11925	~ 15	11 ± 2	...	< 10	~ 15	12.78 ± 0.20	AOD
3C 249.1	0.17371	24 ± 7	29 ± 4	...	< 17	24 ± 7	13.19 ± 0.13	AOD
PG 1116+215	0.05904	~ 27	20 ± 2	~ 19	18 ± 2	~ 24	13.16 ± 0.12	AOD, AOD

several $\log N_i$ bins. The total distribution is then,

$$\mathcal{N}(\log N) = \sum_i \mathcal{N}_i(\log N_i) \quad (2)$$

$$= \sum_i \frac{0.2}{\delta \log N_i \sqrt{2\pi}} \exp\left(\frac{-[\log N - \log N_i]^2}{2[\delta \log N_i]^2}\right).$$

The difference between this distributed-power method and simple histogram binning is subtle; sharp peaks and valleys in the simple histogram are smoothed to some degree, but the general shape remains unchanged. We believe this method takes measurement uncertainty into better account.

At low column densities we must correct the survey

for incompleteness (Papers 1 and 2). To do so, we divide the number of absorbers of a given equivalent width W by an “effective redshift pathlength”, $\Delta z_{\text{eff}}(W)$, which accounts for absorption-line sensitivity. For each species, we calculate the number of absorbers per unit redshift, dN/dz , as a function of column density, N , to account for incompleteness in the weaker absorbers,

$$\frac{dN(\log N)}{dz} = \sum_i \frac{\mathcal{N}_i(\log N_i)}{\Delta z_i}. \quad (3)$$

We measured the sensitivity by the signal-to-noise ratio, S/N , determined for each sight line as the ratio of mean flux to standard deviation in the flux in the line-free continuum of each 10 Å segment of *FUSE* or STIS

TABLE 7
SAMPLE C III DETECTIONS

Sight Line	z_{abs}	$W_r(977)$ (mÅ)	$b(\text{C III})$ (km s $^{-1}$)	$\log N(\text{C III})$ (N in cm $^{-2}$)	notes
HE 0226–4410	0.20700	219 \pm 66	23 \pm 5	13.98 \pm 0.24	fit
HE 0226–4410	0.34031	23 \pm 3	32 \pm 4	12.63 \pm 0.10	AOD
PKS 0312–770	0.20192	270 \pm 17	57 \pm 4	13.63 \pm 0.20	AOD
PKS 0312–770	0.20275	600 \pm 35	94 \pm 5	13.97 \pm 0.35	AOD
PKS 0405–123	0.16714	369 \pm 73	16 \pm 2	14.78 \pm 0.71	fit
PKS 0405–123	0.33400	36 \pm 4	38 \pm 2	12.82 \pm 0.07	AOD
PKS 0405–123	0.36079	141 \pm 10	17 \pm 1	13.61 \pm 0.05	fit
HS 0624+6907	0.32088	10 \pm 3	12 \pm 4	12.10 \pm 0.13	fit
PG 0953+414	0.06808	112 \pm 20	28 \pm 4	13.35 \pm 0.06	fit
PG 0953+414	0.11827	36 \pm 3	26 \pm 8	12.83 \pm 0.09	AOD
PG 0953+414	0.14232	30 \pm 16	20 \pm 12	12.65 \pm 0.19	fit

TABLE 8
SAMPLE Si IV DETECTIONS

Sight Line	z_{abs}	$b(1394)$ (km s $^{-1}$)	$W_r(1394)$ (mÅ)	$b(1403)$ (km s $^{-1}$)	$W_r(1403)$ (mÅ)	$b(\text{Si IV})$ (km s $^{-1}$)	$\log N(\text{Si IV})$ (N in cm $^{-2}$)	notes
PKS 0312–770	0.20192	35 \pm 8	177 \pm 54	40 \pm 2	80 \pm 7	36 \pm 8	13.39 \pm 0.11	fit, AOD
PKS 0312–770	0.20275	76 \pm 3	595 \pm 99	75 \pm 1	470 \pm 12	75 \pm 3	14.17 \pm 0.19	fit, AOD
PKS 0405–123	0.16714	33 \pm 2	164 \pm 12	25 \pm 3	117 \pm 21	30 \pm 4	13.38 \pm 0.09	fit, fit
HS 0624+6907	0.06348	24 \pm 2	47 \pm 4	...	< 54	24 \pm 2	12.80 \pm 0.10	AOD
PG 1116+215	0.13850	17 \pm 1	34 \pm 2	...	< 30	17 \pm 1	12.69 \pm 0.08	AOD
PG 1211+143	0.05104	15 \pm 1	73 \pm 5	17 \pm 1	45 \pm 4	15 \pm 1	13.02 \pm 0.03	fit, fit
Mrk 205	0.00443	30 \pm 1	115 \pm 9	24 \pm 9	74 \pm 7	28 \pm 9	13.30 \pm 0.06	AOD, AOD
Q 1230+0115	0.07805	\sim 10	29 \pm 4	\sim 20	24 \pm 4	\sim 13	12.70 \pm 0.16	AOD, AOD
PG 1259+593	0.23951	10 \pm 8	37 \pm 30	10 \pm 8	12.61 \pm 0.29	fit
PKS 1302–102	0.04225	\sim 18	18 \pm 2	...	< 45	\sim 18	12.39 \pm 0.23	AOD
PKS 1302–102	0.09485	\sim 18	18 \pm 7	...	< 12	\sim 18	12.36 \pm 0.27	AOD

TABLE 9
SAMPLE Si III DETECTIONS

Sight Line	z_{abs}	$W_r(1207)$ (mÅ)	$b(\text{Si III})$ (km s $^{-1}$)	$\log N(\text{Si III})$ (N in cm $^{-2}$)	notes
HE 0226–4410	0.16340	19 \pm 1	\sim 9	12.07 \pm 0.09	AOD
HE 0226–4410	0.19859	20 \pm 3	26 \pm 3	12.07 \pm 0.12	AOD
HE 0226–4410	0.20700	49 \pm 3	24 \pm 4	12.47 \pm 0.05	AOD
HE 0226–4410	0.30565	30 \pm 7	12 \pm 7	12.29 \pm 0.11	AOD
PKS 0312–770	0.05946	21 \pm 5	21 \pm 6	12.07 \pm 0.15	AOD
PKS 0312–770	0.17976	13 \pm 8	8 \pm 5	11.77 \pm 0.21	fit
PKS 0312–770	0.20192	123 \pm 5	30 \pm 1	12.97 \pm 0.05	AOD
PKS 0312–770	0.20275	647 \pm 151	36 \pm 2	14.92 \pm 0.27	fit
PKS 0405–123	0.16714	266 \pm 12	30 \pm 1	13.34 \pm 0.02	fit
PKS 0405–123	0.21070	104 \pm 12	40 \pm 9	12.86 \pm 0.05	AOD
PKS 0405–123	0.35210	128 \pm 17	36 \pm 4	12.74 \pm 0.05	fit

data. In regions of overlapping data (e.g., the overlap of *FUSE* LiF1 and LiF2 channels or the overlap between *FUSE* and STIS/E140M coverage), we used the higher S/N value. The vector, $(S/N)_\lambda$, for a given wavelength λ was rebinned to a resolution comparable to that of the data.

We then modified $(S/N)_\lambda$ to take into account regions in which IGM absorption lines would not be detected. We used two methods to assess the sensitivity of the effective pathlength, Δz , to different $(S/N)_\lambda$ algorithms. In the first method, we set $(S/N)_\lambda = 0$ in ~ 50 regions of strong interstellar lines and instrumental artifacts that appear in most or all of the data sets. In the second method, we let the smoothed, normalized flux

data mask the $(S/N)_\lambda$ profile. Regions of strong absorption ($\tau_\lambda \gg 1$) were completely masked, $(S/N)_\lambda = 0$, while areas of unsaturated absorption were masked proportional to the optical depth, $(S/N)_\lambda \propto (\tau_\lambda + 1)^{-1}$. This effectively removed fixed ISM lines and instrumental artifacts, as well as strong IGM lines and intrinsic AGN features. It also accounted for degraded sensitivity in regions with moderately strong absorption lines of any type (AGN, IGM, or ISM).

Next, we converted each $(S/N)_\lambda$ vector to a 4σ minimum equivalent-width vector using equation 1. For single lines, we determined the total redshift pathlength, $\Delta z(W)$, at a given equivalent width sensitivity by summing the available pathlength over which $W_\lambda > W_{\text{min}}$

TABLE 10
SAMPLE Fe III DETECTIONS

Sight Line	z_{abs}	$W_{\text{r}}(1123)$ (mÅ)	$b(\text{Fe III})$ (km s $^{-1}$)	$\log N(\text{Fe III})$ (N in cm $^{-2}$)	notes
HE 0226–4410	0.16236	23 ± 4	~ 20	13.64 ± 0.14	AOD
PKS 0312–770	0.20192	20 ± 7	6 ± 2	13.52 ± 0.11	fit
PKS 0312–770	0.20275	127 ± 5	64 ± 1	14.46 ± 0.04	AOD
PKS 0405–123	0.16714	22 ± 5	10 ± 2	13.56 ± 0.09	fit
PKS 0405–123	0.35210	28 ± 15	16 ± 6	13.58 ± 0.17	fit
3C 249.1	0.10834	15 ± 1	~ 17	13.47 ± 0.22	AOD
3C 249.1	0.14183	36 ± 4	19 ± 5	13.85 ± 0.08	AOD
3C 249.1	0.24396	16 ± 3	~ 4	13.63 ± 0.12	AOD
PG 1116+215	0.13850	14 ± 1	~ 9	13.44 ± 0.10	AOD
PKS 1302–102	0.07695	24 ± 3	~ 18	13.69 ± 0.13	AOD
Mrk 876	0.11487	25 ± 7	16 ± 5	13.60 ± 0.11	fit

in all 28 sight lines. For multiplet lines, including Ly α and Ly β , we scaled a second vector, $W_{\text{min}}(z)$, by the line-strength ratio, $f\lambda$, and shifted to the rest frame of the weaker line. In this case, $\Delta z(W)$ is the sum of all available pathlength for which either $W_\lambda > W_{\text{min}}(z_1)$ or $W_\lambda > [W_{\text{min}}(z_2)](f_1\lambda_1/f_2\lambda_2)$. In all cases, we excluded pathlength within $\Delta z < 0.005$ (1500 km s $^{-1}$) of the intrinsic AGN redshift and within $\Delta z < 0.0017$ (500 km s $^{-1}$) of the Local Standard of Rest (LSR). Thus, systems intrinsic to the AGN (outflows) or to our Galaxy (high velocity clouds) were not included.

Tripp et al. (2008) study both intrinsic and intervening systems and adopt a more restrictive velocity limit ($\Delta z > 0.017$, $v > 5000$ km s $^{-1}$) than we use here. As they note, there are numerous examples of high- z quasars where intrinsic absorption components are seen at $v > 5000$ km s $^{-1}$. They find the line density for intrinsic absorbers is roughly a factor of two higher than for intervening systems. Nevertheless, Tripp et al. note that the excess of systems is largely confined to the velocity range $-1000 \lesssim v_{\text{displ}} \lesssim 2500$ km s $^{-1}$ and that intrinsic systems are relatively rare at $v_{\text{displ}} > 2500$ km s $^{-1}$.

Both methods of $(S/N)_\lambda$ masking reduced the total Δz in the data by 3–4% relative to the unmasked S/N profile. However, the difference in total Δz between these two methods was less than 1%. The second, self-masking method allocates relatively less pathlength for weak lines and relatively more for stronger lines. We deemed this method to be more realistic and used it throughout our analysis.

In our previous work, the absorber redshifts were generally small and the redshift is linearly proportional to comoving distance, $d\ell = (c/H_0) dz$. In the new survey, we included absorbers out to redshifts $z = 0.4$, where a given a linear distance $d\ell$ covers a larger redshift interval dz than at $z = 0$. We therefore use the relations,

$$\begin{aligned} \frac{d\ell}{dz} &= \frac{1}{(1+z)} \frac{c}{H(z)} \\ &= \frac{c}{H_0} \frac{1}{(1+z)} [\Omega_m(1+z)^3 + \Omega_\Lambda]^{-1/2}, \end{aligned} \quad (4)$$

where we assumed a flat (Ω_m, Λ) cosmology with $H(z) = H_0 [\Omega_m(1+z)^3 + \Omega_\Lambda]^{1/2}$. By including the $(1+z)^3$ density scaling and normalizing to H_0 , it is conventional (Bahcall & Peebles 1969) to define the dimensionless “absorption pathlength function”, $dX = [H_0/H(z)](1 +$

$z)^2 dz$, so that

$$dX \equiv (1+z)^2 [\Omega_m(1+z)^3 + \Omega_\Lambda]^{-1/2} dz. \quad (5)$$

We calculated $\Delta X(N_{\text{min}})$ from the individual spectra in the same manner as $\Delta z(N_{\text{min}})$ above using numerical integration and adopting $\Omega_m = (0.261 \pm 0.016)h_{70}^{-2}$ and $\Omega_\Lambda = 0.716 \pm 0.055$ (Spergel et al. 2007). For low-redshift absorbers, such as all C IV detections ($z_{\text{abs}} \leq 0.11$), the difference between Δz and ΔX is negligible. We list both dN/dz and dN/dX in the discussion, to provide both observational and theoretical perspectives.

Uncertainties in dN/dz arise as uncertainties in both N and Δz . In the numerator, one-sided Poisson statistics (Gehrels 1986) for dN_i are assumed. While the uncertainty in $\Delta z(W)$ is negligible as discussed above, we must still take into account the changing Δz over the width of a column density bin. For weak lines where the $\Delta z_{\text{eff}}(W)$ is falling sharply, there is a significant difference in Δz between one side of an equivalent width or column density bin and the other. We approximate this uncertainty as $d\Delta z_i = \frac{1}{8}[(\Delta z)_{i+1} - (\Delta z)_{i-1}]$ or roughly the change in Δz over a quarter of a bin, the typical 1σ dispersion of column densities from bin center. The dN/dz uncertainties from numerator and denominator are added in quadrature. Uncertainty from Poisson statistics dominates in almost all cases, but $d\Delta z_i$ becomes significant for numerous absorbers (H I, O VI, Si III) in the weakest column density bins. Uncertainties in dN/dX are completely analogous.

2.5. Baryon Fraction

Through measurements of D/H and acoustic peaks in the CMB, we now have an accurate estimate of the cosmological density of baryons, $\Omega_b h_{70}^2 = 0.0455 \pm 0.0015$ (Spergel et al. 2007). However, most of these baryons do not exist in collapsed form, and probably are distributed throughout various phases of the IGM (Cen & Ostriker 1999; Shull 2003). This is certainly the case at high redshift, where the Ly α forest is the repository for large quantities of gas that has not yet collapsed into galaxies. But even at low redshifts, the IGM likely contains between 50% and 80% of the baryonic matter. Because low-density gas at a variety of temperatures can be difficult to detect, a complete cosmological baryon census requires a combination of ultraviolet and X-ray spectrographs.

Here, we use UV spectroscopic column densities and

absorber frequencies of H I and various metal ions to derive the baryon density contained in IGM thermal phases at $T \leq 10^6$ K. To compare to similar estimates in the literature, it is convenient to define two such measures. The first, directly measured quantity provides the contribution to the critical mass density, of the IGM absorber mass in a given ion,

$$\Omega_{\text{ion}} = \left(\frac{H_0 m_{\text{ion}}}{c \rho_{\text{cr},0}} \right) \times \int_{N_{\text{min}}}^{N_{\text{max}}} \left[\frac{d\mathcal{N}(\log N_{\text{ion}})}{dX} \right] \langle N_{\text{ion}} \rangle d \log N_{\text{ion}}. \quad (6)$$

The integration is over the column density distribution and the corrected redshift pathlength parameter dX . Here, m_{ion} is the ion mass, and the critical density is $\rho_{\text{cr},0} = (3H_0^2/8\pi G) = (1.879 \times 10^{-29} \text{ g cm}^{-3})h^2$. The integration is over the column density distribution and the corrected redshift pathlength parameter dX .

Uncertainty in Ω_{ion} is taken as the asymmetric Poisson uncertainty on $d\mathcal{N}(N)$ evaluated at a $d\mathcal{N}$ -weighted mean dX , $\langle z \rangle$, and $\langle N \rangle$. The value of $\Omega_{\text{ion}} \propto [Z(M/H)_{\odot} f_{\text{ion}} h_{70}]^{-1}$, so we do not include systematic uncertainties in these quantities. Non-equilibrium ionization may produce higher ion fractions for Si IV and the Li-like ions while photoionization may lower the assumed near-unity CIE ion fractions of C III, Si III, and Fe III. Similarly non-solar abundance ratios or deviations from the canonical 10% solar metallicity often assumed for IGM clouds will introduce systematic differences.

The second parameter, $\Omega_{\text{IGM}}^{(\text{ion})}$, estimates the density of *all* baryons traced by the particular ion after correcting for abundances and ionization stages. In Paper 1, we calculated the fraction of the universe composed of baryons at $T = 10^{5-6}$ K, using O VI as a tracer for baryonic WHIM gas in general. This parameter includes corrections for the metallicity, Z , of the element relative to solar abundances, and for the ionization fraction, f_{OVI} , of the particular ion. Our adopted formula was

$$\Omega_{\text{IGM}}^{(\text{OVI})} = \left(\frac{H_0}{c \rho_{\text{cr},0}} \right) \frac{\mu m_H}{Z(O/H)_{\odot} f_{\text{OVI}}} \times \int_{N_{\text{min}}}^{N_{\text{max}}} \left[\frac{d\mathcal{N}(\log N_{\text{OVI}})}{dz} \right] \langle N_{\text{OVI}} \rangle d \log N_{\text{OVI}}, \quad (7)$$

where $\mu = 1.32$ for low-metallicity gas and primordial helium, $Y_p \approx 0.2477 \pm 0.0029$ (Peimbert et al. 2007).

We can easily generalize this formula for any ion dividing Ω_{ion} by an assumed metallicity, $Z = 0.1 Z_{\odot}$, abundance of element M relative to hydrogen, $(M/H)_{\odot}$, and ionization fraction (assumed to be the peak CIE ion abundance f_{ion} listed in Table 3). Because the redshift range in our current work is larger than that covered in Paper 1, we adopt pathlength coordinate X instead of z , as discussed above, and we perform the sum over bins of equal ΔX .

$$\Omega_{\text{IGM}}^{(\text{ion})} = \left(\frac{H_0}{c \rho_{\text{cr},0}} \right) \frac{\mu m_H}{Z(M/H)_{\odot} f_{\text{ion}}} \times \int_0^{X_{\text{max}}} \int_{N_{\text{min}}}^{N_{\text{max}}} \left[\frac{d\mathcal{N}_{\text{ion}}(\log N_{\text{ion}})}{dX} \right] \langle N_{\text{ion}} \rangle d \log N_{\text{ion}} dX$$

$$\Omega_{\text{IGM}}^{(\text{ion})} = \frac{1.83 \times 10^{-23} h_{70}^{-1} \text{ cm}^2}{Z(M/H)_{\odot} f_{\text{ion}}} \times \quad (8)$$

$$\sum_{j=0}^{X_{\text{max}}} \sum_{i=N_{\text{min}}}^{N_{\text{max}}} \left[\frac{d\mathcal{N}(\log N_{\text{ion}})}{dX} \right]_{i,j} \frac{\langle N_{\text{ion}} \rangle_{i,j} \Delta \log N_{\text{ion}} \Delta X_j}{X_{\text{max}}}.$$

As in our previous work, we adopt a fiducial IGM metallicity of $Z = 0.1 Z_{\odot}$ and a Hubble constant $H_0 = (70 \text{ km s}^{-1} \text{ Mpc}^{-1})h_{70}$. We sum $d\mathcal{N}/dX$ for each ion over bins in column density N_{ion} and normalized pathlength dX . The final term, $\Delta X_j/X_{\text{max}}$, averages the $d\mathcal{N}/dX$ contributions from each dX bin.

2.5.1. Baryons in the Ly α Forest

While the main focus of this paper is metal ions, our database of H I absorbers is the largest to date in the low- z IGM and can provide good constraints on $\Omega_{\text{IGM}}^{(\text{HI})}$, the fraction of IGM baryons in the Ly α forest. For this we use the methods of Penton, Shull, & Stocke (2000) and Schaye (2001), which are slightly different from the methods employed for $\Omega_{\text{IGM}}^{(\text{ion})}$ above. In the first method, the IGM absorbers are assumed to be isothermal spheres, and the total cloud mass is inferred from the H I column density and an assumed impact parameter. The neutral fraction is derived from photoionization conditions. Following Penton, Shull, & Stocke (2000), we define

$$\Omega_{\text{IGM}}^{(\text{HI})} = \frac{(1.59 \times 10^9 M_{\odot}) H_0 [\ell_{100}^5 J_{-23} (\frac{4.8}{\alpha_s + 3})]^{1/2}}{c \pi \ell^2 \rho_{\text{cr}}} \times \int_{N_{\text{min}}}^{N_{\text{max}}} \frac{d\mathcal{N}(N_{\text{HI}})}{dz} N_{14}^{1/2} dN_{\text{HI}}$$

$$\Omega_{\text{IGM}}^{(\text{HI})} = 8.73 \times 10^{-5} h_{70}^{-1} \left[J_{-23} \ell_{100} \frac{4.8}{\alpha_s + 3} \right]^{1/2} \times \sum_{X=0}^{X_{\text{max}}} \sum_{\log N_{\text{min}}}^{\log N_{\text{max}}} \frac{d\mathcal{N}(\log N_{\text{HI}})}{dz} N_{14}^{1/2} \frac{\Delta X}{X_{\text{max}}}, \quad (9)$$

where ℓ_{100} is the typical scale of Ly α forest clouds scaled to 100 kpc, J_{-23} is the ionizing radiation field intensity at low redshift (Shull et al. 1999) in units of $10^{-23} \text{ ergs cm}^{-2} \text{ s}^{-1} \text{ Hz}^{-1} \text{ sr}^{-1}$, α_s is the spectral index of the radiation field above 1 ryd scaled to $\alpha_s = 1.8$, and N_{14} is the H I column density in units of 10^{14} cm^{-2} . Secondly, we use the formalism of Schaye (2001), which assumes that IGM clouds are gravitationally bound and that their observed column densities are typical over a Jeans length:

$$\Omega_{\text{IGM}}^{(\text{HI})} = (1.46 \times 10^{-4}) h_{70}^{-1} \Gamma_{-12}^{1/3} T_4^{0.59} \times \int_{N_{\text{min}}}^{N_{\text{max}}} \frac{d\mathcal{N}(N_{\text{HI}})}{dz} N_{14}^{1/3} dN_{\text{HI}}$$

$$\Omega_{\text{IGM}}^{(\text{HI})} = (1.46 \times 10^{-4}) h_{70}^{-1} \Gamma_{-12}^{1/3} T_4^{0.59} \times \sum_{X=0}^{X_{\text{max}}} \sum_{\log N_{\text{min}}}^{\log N_{\text{max}}} \frac{d\mathcal{N}(\log N_{\text{HI}})}{dz} N_{14}^{1/3} \frac{\Delta X}{X_{\text{max}}}. \quad (10)$$

As with Ω_{ion} , we perform a two-dimensional sum over both column density and redshift bins assuming $T = 2 \times 10^4$ K in the photoionized gas and a hydrogen photionization rate $\Gamma_{\text{HI}} = 0.03 \times 10^{-12} \text{ s}^{-1}$

TABLE 11
IGM DETECTIONS AND RESULTS SUMMARY

ion	\mathcal{N}	z_{abs}	Δz_{max}	α_{14}	C_{14}	$Z/26$
O VI	83	< 0.40	5.22	0.71 ± 0.03	2.0 ± 0.1	$0.15^{+0.03}_{-0.02}$
N V	24	< 0.396	5.30	0.98 ± 0.07	5.3 ± 0.7	$0.39^{+0.05}_{-0.04}$
C IV	24	< 0.116	2.42	0.87 ± 0.06	5.5 ± 0.7	$0.055^{+0.007}_{-0.005}$
C III	39	< 0.40	4.84	0.56 ± 0.05	9.5 ± 0.9	$0.015^{+0.001}_{-0.001}$
Si IV	20	< 0.24	4.21	0.74 ± 0.06	12 ± 2	$0.19^{+0.03}_{-0.02}$
Si III	53	< 0.40	5.14	0.81 ± 0.03	41 ± 3	$0.023^{+0.002}_{-0.002}$
Fe III	14	< 0.40	5.11	0.71 ± 0.05	1.6 ± 0.2	$0.7^{+0.1}_{-0.1}$
H I	650	< 0.40	5.27
Previous Work/Literature Values						
O VI	40	< 0.15	2.21	0.9 ± 0.1	2.5 ± 0.2	$0.09^{+0.03}_{-0.02}$
O VI	44	0.12–0.57	~ 1.9	$0.23^{+0.03}_{-0.02}$
O VI	53	< 0.5	3.18	~ 0.9	~ 2	$0.11^{+0.03}_{-0.02}$
C III	30	< 0.21	2.41	0.73 ± 0.08	11.5 ± 1.0^d	$0.016^{+0.002}_{-0.001}$
H I	187	< 0.069	0.770
This Work - Equivalent Sample						
O VI	35	< 0.15	2.96	0.81 ± 0.06	1.96 ± 0.19	$0.11^{+0.03}_{-0.02}$
C III	28	< 0.21	3.485	0.65 ± 0.05	7.69 ± 0.91	$0.016^{+0.002}_{-0.001}$

^a Scaled by f_{ion} , the maximum CIE abundance (Sutherland & Dopita 1993). ^b Number of absorbers per unit pathlength (dX) integrated down to equivalent width $W > 30 \text{ mÅ}$. ^c 1-this work; 2-Danforth et al. 2006; 3-Penton et al. 2004^d Published value of parameter C_{14} (Paper 2), and hence $ZC = 12\%$ were incorrect. Corrected values are listed here.

(Shull et al. 1999; Weymann et al. 2001). Uncertainties in $\Omega_{\text{IGM}}^{(\text{HI})}(\log N)$ are the quadratic sum of the one-sided Poisson error for total redshift pathlength $dN(d \log N, dX)$. Penton, Stocke, & Shull (2004) showed that uncertainty due to cosmic variance is small relative to Poisson error for $\Delta z \gtrsim 1$. Since we are summing over $\Delta z > 5$ for all but the lowest column density bins, we discount cosmic variance as a significant source of error.

3. RESULTS AND DISCUSSION

In Table 11, we present a compilation of our results. The first three columns list ion name, total number of detections (at *any* equivalent width), and redshift coverage of the survey. Column 4 lists the maximum total redshift pathlength sampled to *any* sensitivity; because of (S/N) dependence, a smaller total pathlength is sensitive to weaker absorbers.

For each ion, we produce a plot of the “multiphase ratio”, $\log(N_{\text{HI}}/N_{\text{ion}})$ vs. $\log N_{\text{HI}}$. This ratio was initially defined for O VI (Paper 1) to characterize the potential connections between different tracers of baryonic mass (H I and O VI) observed to be kinematically associated in the low- z IGM. We assume that absorbing clouds in the IGM have both a photoionized component (traced by sharp Ly α lines and low-ionization metal ions) and shock-heated gas (WHIM, traced by O VI or other high-ions). Collisionally ionized C III, Si III, etc. are possible, but we consider this less common due to the fast cooling rates at $T < 10^5 \text{ K}$, where these ions reach their peak CIE abundance (see Paper 2 for discussion). In columns 5 and 6, we list the slope, α_{14} , and the intercept, C_{14} , at column density $N_{\text{HI}} = 10^{14} \text{ cm}^{-2}$ of an error-weighted linear fit to the multiphase correlation. These two parameters are used, together with various

assumptions about ionization corrections, to infer a statistical metallicity of the IGM (see the derivations and discussion in Papers 1 and 2). We quote each metallicity as a fraction of the solar abundance (Asplund et al. 2005) and scale them by f_{ion} , the peak ion abundance in collisional ionization equilibrium (Sutherland & Dopita 1993) or in photoionization equilibrium (see Table 3). Our inferred metallicities are an average for the entire sample; we make no claims as to the metallicity of individual absorbers. The observed doubly-ionized species (C III, Si III, Fe III) have peak CIE abundances close to unity, so these metallicity values are probably lower limits. The ion Si IV and the Li-like ions (C IV, N V, O VI) have peak CIE ionization fractions $f_{\text{peak}} \sim 0.2 - 0.3$.

In column 8, we provide the total absorber frequency per unit redshift, dN/dz , integrated down to fiducial equivalents with 30 mÅ (the survey goes deeper than this limit in many cases). Column 9 gives values of the proper-length corrected dN/dX for $W \geq 80 \text{ mÅ}$. The cumulative bivariate distribution of absorbers per redshift interval as a function of column density was fitted with a power law, $[dN/dz > N] \propto N^{-\beta}$, and the index β is listed in column 10. The power-law slope becomes systematically steeper by 0.05–0.1 dex when using traditional histogram techniques, as some of the data is scattered to the high and low ends of the distribution using our “distributed power” technique. We determined β by an error-weighted fit to the cumulative dN/dz . However, the index fitted to cumulative dN/dX is comparable, within the uncertainties in all cases.

Where possible, Table 11 lists the equivalent values from Papers 1 and 2, as well as several other large surveys of the low- z IGM. For direct comparison of the current survey to our previous work, we calculate O VI statistics for $z < 0.15$ and C III statistics for $z < 0.21$, consistent with the limits in Papers 1 and 2, respectively. We have not adopted the $W_{\text{Ly}\alpha} > 80 \text{ mÅ}$ criterion used in those papers, nor have we accounted for the somewhat less stringent detection requirements adopted in our earlier work (detections in Papers 1 and 2 were 3σ , while the current work requires a minimum of 4σ).

We continue our results in Table 12, listing Ω_{ion} and $\Omega_{\text{IGM}}^{(\text{ion})}$ for absorbers with equivalent width limits $W_{\lambda} > 10 \text{ mÅ}$ and $W_{\lambda} > 30 \text{ mÅ}$. The $\Omega_{\text{IGM}}^{(\text{ion})}$ values are relative to the fiducial baryon fraction $\Omega_{\text{baryon}} = 0.0455 h_{70}^{-2}$ (Spergel et al. 2007) and are scaled by $(f_{\text{peak}}/f_{\text{ion}})(Z/0.1)^{-1} h_{70}^{-1}$ as described above. As in Table 11 above, we list related values from previous surveys and compare to equivalent values from previous surveys.

3.1. Discussion of Individual Species

3.1.1. H I

Our new H I results (Figure 3) are compatible with previous studies. Penton, Stocke, & Shull (2004) found $dN/dz \approx 165 \pm 15$ for Ly α absorbers down to $W_{\lambda} = 30 \text{ mÅ}$ equivalent width, with a median $W_{\text{Ly}\alpha} = 68 \text{ mÅ}$ and a power-law distribution in column density $dN(N)/dz \propto N^{-\beta}$ with $\beta_{\text{HI}} = 1.65 \pm 0.07$. In Paper 2, we searched for O VI and C III absorbers in Ly α systems with $W_{\text{Ly}\alpha} \geq 80 \text{ mÅ}$, correcting for Ly α saturation with full CoG determinations of column density in most cases.

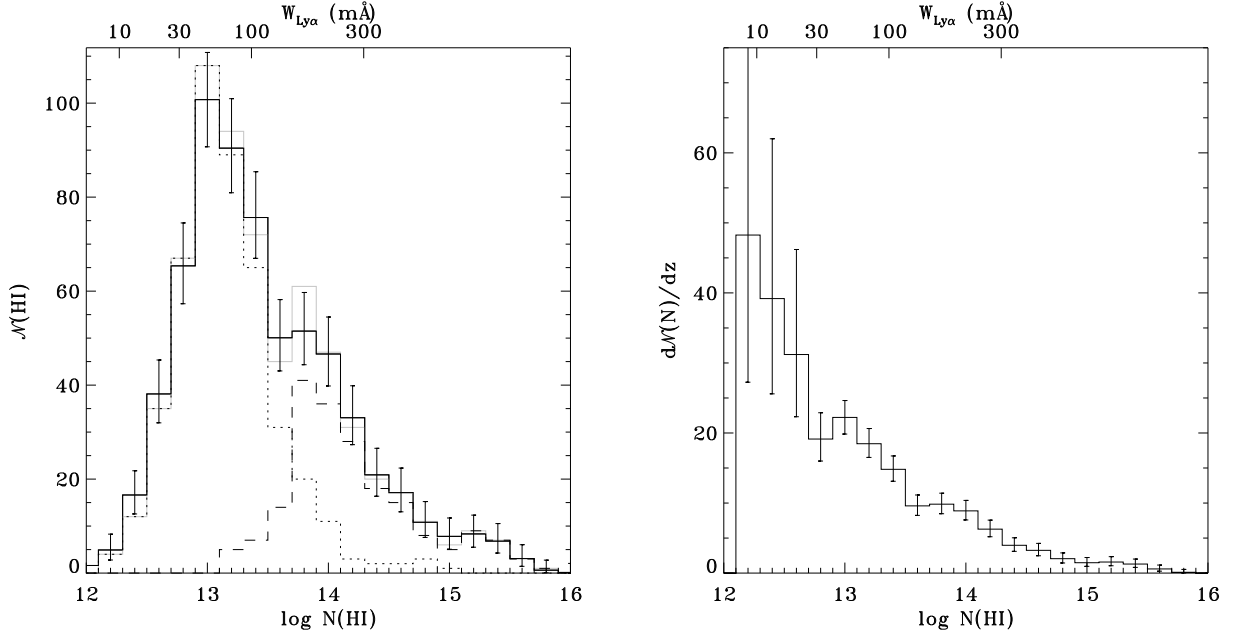


FIG. 3.— HI detection statistics and dN/dz . Left panel shows the number of HI absorbers per logarithmic bin, $\Delta \log N_{\text{HI}} = 0.2$, uncorrected for completeness. Note the turnover at $\log N_{\text{HI}} < 13$. Dashed curve shows absorbers for which higher-order Lyman lines were used to constrain the $(N_{\text{HI}}, b_{\text{HI}})$ solution. Dotted curve shows Ly α -only solutions. Right panel shows completeness-corrected differential dN/dz vs. N_{HI} . Error bars on the left panel are based on one-sided Poisson counting errors (Gehrels 1986), while the error in dN/dz includes a component of Δz uncertainty as well. See text for discussion.

TABLE 12
 Ω_{ion} AND $\Omega_{\text{IGM}}^{(\text{ion})}$ SUMMARY

ion	$\Omega_{\text{ion}} [10^{-8}]$ ($> 10 \text{ m}\text{\AA}$)	$\Omega_{\text{ion}} [10^{-8}]$ ($> 30 \text{ m}\text{\AA}$)	$\Omega_{\text{IGM}}^{(\text{ion})}/\Omega_{\text{b}}^{\text{a}}$ ($> 10 \text{ m}\text{\AA}$)	$\Omega_{\text{IGM}}^{(\text{ion})}/\Omega_{\text{b}}^{\text{a}}$ ($> 30 \text{ m}\text{\AA}$)	Source ^b
O VI	49 ± 4	41 ± 5	0.086 ± 0.008	0.073 ± 0.008	1
N V	3.6 ± 0.8	3.0 ± 0.9	0.050 ± 0.011	0.042 ± 0.012	1
C IV	8.2 ± 1.4	7.7 ± 1.5	0.027 ± 0.005	0.026 ± 0.005	1
C III	8.9 ± 1.3	7.8 ± 1.4	0.010 ± 0.002	0.009 ± 0.002	1
Si IV	8.4 ± 1.1	8.3 ± 1.1	0.075 ± 0.010	0.075 ± 0.010	1
Si III	11 ± 2	10 ± 2	0.037 ± 0.006	0.037 ± 0.007	1
Fe III	20 ± 5	11 ± 7	0.040 ± 0.011	0.022 ± 0.015	1
Previous Work/Literature Values					
O VI ($z < 0.15$)	...	26 ± 4	...	0.048 ± 0.007	2
O VI ($z > 0.12$)	0.059	3
This Work - Equivalent Sample					
O VI ($z < 0.15$)	49 ± 4	33 ± 5	0.087 ± 0.008	0.058 ± 0.008	1

^a Scaled by f_{ion} , the maximum CIE abundance (Sutherland & Dopita 1993), $Z = 0.1 Z_{\odot}$, and $H_0 = 70 \text{ km s}^{-1} \text{ Mpc}^{-1}$. $\Omega_{\text{b}} = 0.0455 \pm 0.0015 h_{70}^{-2}$ (Spergel et al. 2007). See text.^b 1-this work; 2-Danforth & Shull 2005; 3-Tripp et al. 2005

Despite this correction for artificially low values of N_{HI} , we found only a minor change in index, $\beta_{\text{HI}} = 1.68 \pm 0.11$. In our new work, we do not use a minimum Ly α equivalent width, but rather are limited only by the quality of the data. We find a survey median of $W_{\text{Ly}\alpha} = 94 \text{ m}\text{\AA}$, with the uncorrected distribution peaked at $W_{\text{Ly}\alpha} \sim 45 \text{ m}\text{\AA}$. The power-law index is $\beta_{\text{HI}} = 1.73 \pm 0.04$, and the distribution has an integrated line frequency of $dN/dz = 129^{+6}_{-5}$ down to $30 \text{ m}\text{\AA}$, significantly different from the result of Penton, Stocke, & Shull (2004). However, all the absorbers in the Penton et al. surveys were at $z < 0.07$, while those in the current survey are at

$z < 0.4$ (with $\langle z \rangle = 0.14$). The proper-length-corrected absorber frequency is $dN/dX = 151^{+7}_{-6}$, more in line with the Penton, Stocke, & Shull (2004) result.

The N_{HI} histogram and dN/dz plot show a small dip at $\log N_{\text{HI}} = 13.6$ in an otherwise smooth and well-behaved distribution. This is likely a selection effect of how we chose and measured Ly α absorbers. In Paper 2, we showed that H I measurements using only the Ly α line tend to underestimate N_{HI} because of line saturation. The dip at $\log N_{\text{HI}} = 13.6$ lies at the transition between Ly α -only and CoG-determined column densities and is almost certainly an artifact. Since the total number of

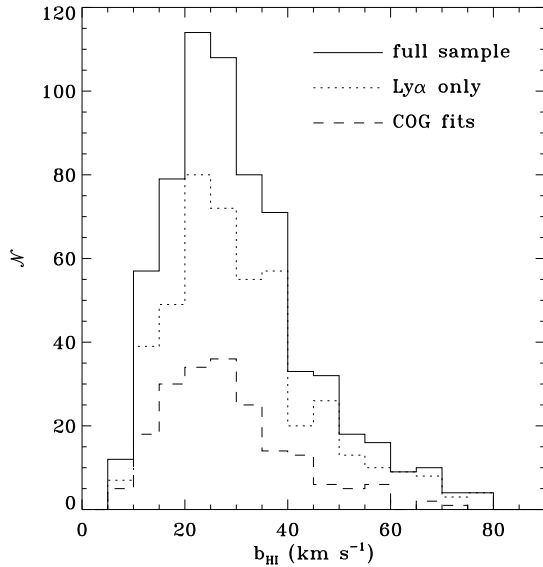


FIG. 4.— Distribution of doppler b -values for 650 H I absorbers. Dashed line represents the subset of 195 systems for which a curve of growth N, b solution is available. Dotted line represents the remainder (455) for which only Ly α fits were used. The median and standard deviations for each sample are 27 ± 15 km s $^{-1}$ (total), 25 ± 13 km s $^{-1}$ (CoG), and 28 ± 16 km s $^{-1}$ (Ly α). Broad Ly α Absorbers (BLAs) $b_{\text{HI}} > 40$ km s $^{-1}$ represent $\lesssim 20\%$ of the absorbers. These may indicate high gas temperatures ($T > 10^5$ K), multiple components, or bulk flows within the absorber. A number of the broadest systems may be multiple blended components (see Shull et al. (2000) and Paper 2 for discussion) so this BLA fraction is probably an upper limit. Compare with Fig. 6 in Paper 2 and Fig. 12 of Tripp et al. (2008).

absorbers is conserved, any effect on β_{HI} , dN/dz , or Ω from this artifact is likely negligible and is unique to the H I data.

Hydrogen is the lightest element and thus is particularly sensitive to thermal broadening. The distribution of doppler parameters, b_{HI} , provides a valuable upper limit on gas temperature. Figure 4 shows the distributions for the entire sample (650 lines) of H I measurements, the corrected Ly α -only (455), and CoG-qualified (195) subsamples. The distributions are similar for each sample, with a median and 1σ variation of 27 ± 15 km s $^{-1}$ (28 ± 16 km s $^{-1}$, 25 ± 13 km s $^{-1}$), consistent with the results of Paper 2. Assuming that the entire line width is due to thermal broadening, $b_{\text{HI}} = 27$ km s $^{-1}$ corresponds to a gas temperature $T = 60.5 b_{\text{HI}}^2 \approx 44,000$ K. However, some of the doppler width is undoubtedly due to velocity components and bulk flows.

Lehner et al. (2007) find a large number of broad Ly α absorbers (BLAs) in many of the same sight lines with $b_{\text{HI}} > 40$ km s $^{-1}$ as measured from Ly α lines. In some cases, they report $b_{\text{HI}} > 100$ km s $^{-1}$. If the line width is entirely due to gas temperature, these measurements imply $T \geq 10^5$ K. However, very broad lines are difficult to detect against all but extremely well-characterized AGN continua and subject to a number of interpretations. Only extremely strong Ly α systems can be both broad and deep at the same time, and these are often not unambiguously a single component. Shallow, broad features are far more common, but may arise from continuum variations or instrumental artifacts such as “echelle

ripples”. We find that 15-20% of our H I systems show $b_{\text{HI}} > 40$ km s $^{-1}$, and the fraction falls off rapidly at higher b_{HI} . The details of these individual detections are beyond the scope of this paper, but we will address these BLA systems in detail in an upcoming paper (Danforth et al., in preparation).

3.1.2. O VI

Our O VI results (Figure 5a,b) are compatible with those in Paper 1. In that work, we found a column density distribution with $\beta_{\text{OVI}} = 2.2 \pm 0.1$, slightly steeper² than seen in the current, larger sample ($\beta_{\text{OVI}} = 1.98 \pm 0.11$). The multiphase slope parameter α_{14} differs between the two samples as well (0.7 vs. 0.9). In Paper 1 we derived $\alpha_{14} = 0.9 \pm 0.1$, consistent with no N_{HI} correlation; but we now find $\alpha_{14} = 0.71 \pm 0.03$ in the larger sample, consistent with some degree of correlation. However, the two studies probe different redshift ranges. If the current sample is limited to $z_{\text{abs}} < 0.15$, as in Paper 1, we have 35 absorbers with $\beta = 2.26 \pm 0.20$ and $\alpha_{14} = 0.81 \pm 0.06$, in closer agreement with Paper 1. This suggests some redshift evolution in the O VI absorbers between $0 < z_{\text{abs}} < 0.4$, as suggested in some simulations of the rate at which the metal-seeded WHIM increases at low redshift (Davé et al. 1999; Cen & Ostriker 1999).

The new sample of O VI absorbers shows a strong power-law distribution (Figure 5b). In Paper 1, we reported hints of a turnover in the dN/dz column-density distribution at $\log N_{\text{OVI}} < 13.4$ ($W_{1032} < 30$ mÅ). However, there were only five absorbers in these low- N bins, and our conclusion was tentative. Our new study features 26 absorbers with $\log N_{\text{OVI}} < 13.4$, and the distribution continues as a smooth power law, with no apparent turnover down to $\log N_{\text{OVI}} \approx 13.0$ ($W_{1032} > 12.5$ mÅ). Even the $z < 0.15$ subsample has six absorbers with $\log N_{\text{OVI}} < 13.4$ and also shows a similarly smooth power law down to $\log N_{\text{OVI}} \sim 13.1$, with no suggestion of a turnover. The continued rise in this distribution can be used to constrain the extent of metal transport away from dwarf galaxies (Stocke et al. 2006b; Tumlinson & Fang 2005).

As in Paper 1, we compare the observed O VI statistics to theoretical predictions. Cen & Fang (2006) compute several different sets of models of the evolution of the WHIM with (and without) realistic galactic superwind (GSW) feedback and with non-equilibrium evolution of major metal ions (including O VI and other WHIM tracers). They compare their models (their Figure 2) to the observed cumulative dN/dz distribution at different O VI equivalent widths (Paper 1). They see reasonably good agreement with the data in the model with GSW and non-equilibrium ionization. In Figure 6, we compare the Cen & Fang (2006) models to the current dN/dz data versus equivalent width. Minimizing the Ly α bias has generally increased dN/dz and now is best described by the GSW model with species in ionization equilibrium. The non-equilibrium model underpredicts O VI absorber density at all column densities. While we do not believe that the models are sufficiently accurate

² Results in Papers 1 and 2 did not use the distributed-power histogram technique reported here. This technique is known to decrease β values by 0.05–0.10 dex, however, we have not adjusted the literature values.

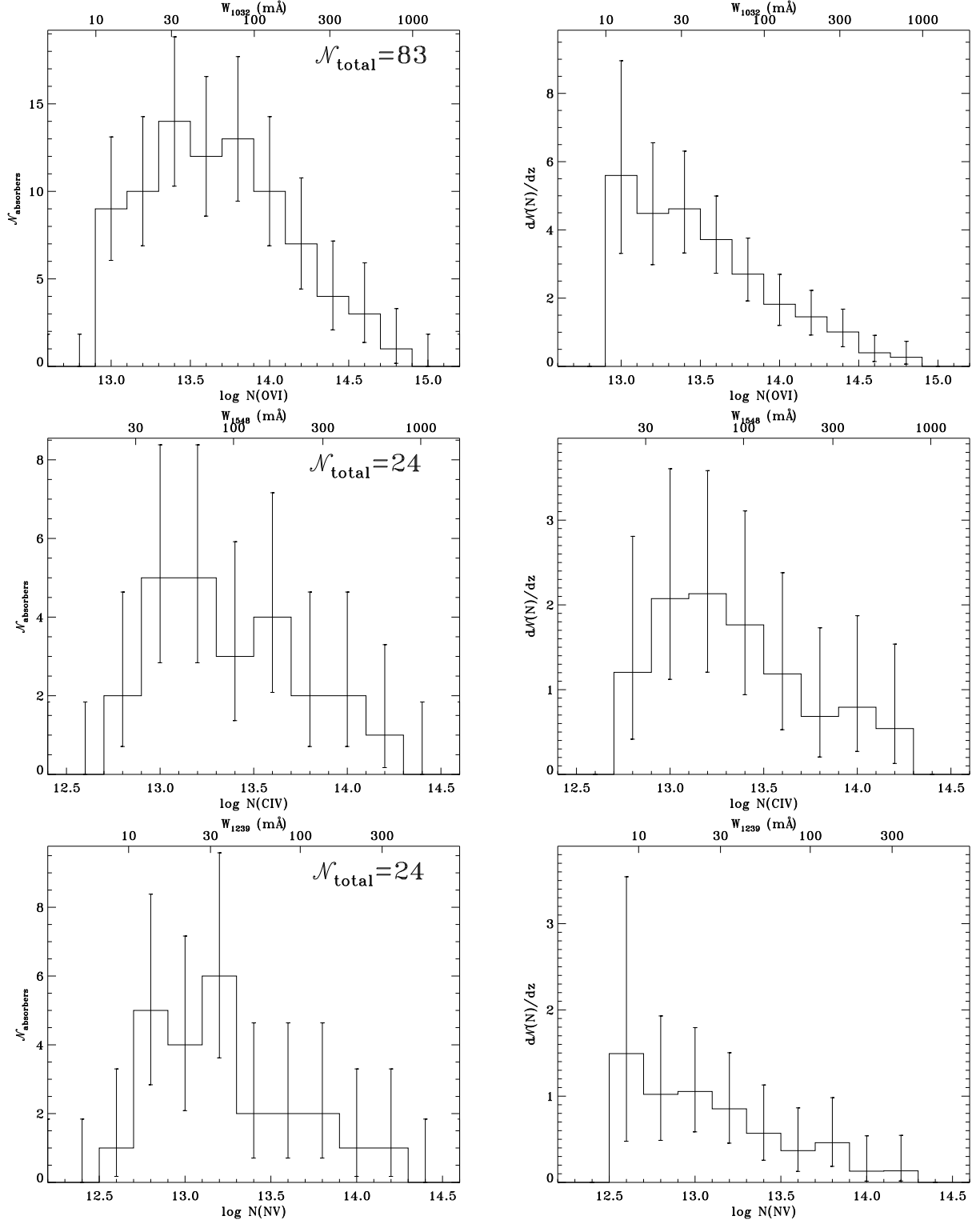


FIG. 5.— Detection statistics and dN/dz for OVI (top), CIV (middle), and NV (bottom). All column densities are measured directly from the data (profile fits or AOD method) and not from curves of growth.

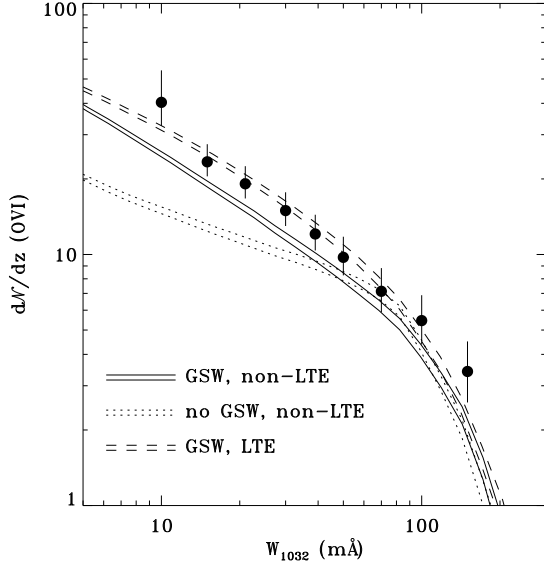


FIG. 6.— Observed cumulative dN/dz for O VI at different equivalent widths, compared with several simulations by Cen & Fang (2006). The simulation labeled LTE (actually collisional ionization equilibrium) and galactic stellar winds (GSW) matches the observations most closely. However, note the slight excess in observed strong systems above $W > 100$ mÅ. This may be due to enhanced metallicity in the strongest systems, or it may be an artifact of the finite size of the simulation volume.

to discriminate between CIE and non-equilibrium ionization, it is clear that GSW are required to produce the observed enhancement in number of weak, low- N_{OVI} absorbers. Changes in metallicity tend to shift the models up and down, and a higher metal production rate might match the observations more closely. There are certain additional systematics which must be mentioned. For instance, the models were calculated at $z = 0$, while our O VI observations are at $\langle z \rangle \sim 0.2$. The WHIM fraction is expected to increase as a function of time (Davé et al. 1999); if the models were integrated over the same redshift range as the observations, they would likely predict lower dN/dz values. Also, if we account for the full O VI census including lines with no measurable Ly α counterpart, the dN/dz values would increase as discussed below. Both of these systematics would decrease the agreement between the data and models.

We see a distribution of O VI b -values that covers a wide range. This distribution is of physical importance, since explaining observed line width as thermal broadening provides an upper limit to the temperature of O VI-bearing gas in the IGM. O VI has a thermal line width

$$b_{\text{OVI}} = \sqrt{\frac{2kT}{m_{\text{O}}}} \approx (17.05 \text{ km s}^{-1}) \left(\frac{T}{T_{\text{max}}} \right)^{1/2}, \quad (11)$$

where $T_{\text{max}} = 10^{5.45}$ K and $m_{\text{O}} = 16 m_{\text{H}}$. Turbulence and unresolved velocity components may artificially broaden the line profiles, but b_{OVI} does provide a useful upper limit to the gas temperature. For the most part, O VI lines were measured by a profile fitting routine that takes instrumental resolution into account. The distribution looks much like those reported in Fig. 12 of Tripp et al. (2008) and in Fig. 6 of Paper 2. Of our 83 O VI detections, only 11 have $b_{\text{OVI}} \geq 50 \text{ km s}^{-1}$ and only four systems have $b_{\text{OVI}} \geq 60 \text{ km s}^{-1}$ (each of these

four systems shows multiple components). The mean is $\langle b_{\text{OVI}} \rangle = 30 \pm 16 \text{ km s}^{-1}$ with a median value lower by 3 km s^{-1} , nearly identical to our results in Paper 2. Nineteen of our absorbers (23%) show $b_{\text{OVI}} \leq 17 \text{ km s}^{-1}$ (temperatures at or below the peak CIE temperature) while only five (6%) show $b_{\text{OVI}} < 10 \text{ km s}^{-1}$, corresponding to $T \leq 10^5$ K, consistent with photoionization. By comparison, Tripp et al. (2008) find that 37% of their intervening O VI systems have $b < 10 \text{ km s}^{-1}$, implying low temperatures in a substantial fraction of their absorbers. As shown by Cen & Fang (2006), one expects some fraction of the WHIM to lie at temperatures below T_{max} , owing to time-dependent radiative cooling to $T \leq 10^5$ K. However, Tripp et al. subdivided many of their absorption systems into individual components, and some of the fits may be artificially narrow.

As in Paper 2, we can use the distribution of H I line b -values to provide an upper bound on the size of IGM clouds. Non-virialized clouds of greater than ~ 1 Mpc extent would show significant Hubble expansion. Assuming that the observed line width is due to instrumental, thermal, and Hubble expansion effects, and that all O VI absorbers exist at their peak CIE temperature, we calculate

$$\langle \ell \rangle \leq [\langle b_{\text{OVI}} \rangle^2 - 17^2]^{1/2} [H(z)]^{-1} \sim 350 h_{70}^{-1} \text{ kpc}, \quad (12)$$

consistent with previous results (Tumlinson & Fang 2005; Danforth et al. 2006). Here, we have accounted for the small increase in Hubble expansion, $H(z) = H_0 [\Omega_m (1+z)^3 + \Omega_\Lambda]^{1/2} \approx 75 \text{ km s}^{-1} \text{ Mpc}^{-1}$, at the mean H I absorber redshift, $\langle z \rangle = 0.14$.

Throughout this analysis, we assume that O VI is predominantly thermally ionized. For photoionization to dominate collisional ionization for O VI, the gas density must be fairly low, $n_{\text{H}} \approx 10^{-6} \text{ cm}^{-3}$. A typical H I absorber has $N_{\text{HI}} \sim 10^{14} \text{ cm}^{-2}$ and, at WHIM temperatures, a neutral fraction $f_{\text{HI}} < 10^{-5}$. This gives a characteristic length scale

$$L_{\text{HI}} = \frac{(N_{\text{HI}}/f_{\text{HI}})}{n_{\text{H}}} \sim (3 \text{ Mpc}) \frac{N_{\text{HI}}}{10^{14} \text{ cm}^{-2}} \quad (13)$$

The high ionization parameter for photoionized O VI requires extremely diffuse clouds ($\delta_{\text{H}} \sim 5$) and thus extremely long pathlengths ($L_{\text{H}} \sim 3 \text{ Mpc}$) for typical observed column densities. The Hubble broadening over this length for an unvirialized cloud, $v_{\text{H}} = L_{\text{HI}} H_0 \approx 200 h_{70} \text{ km s}^{-1}$, is many times larger than the observed line widths of any observed absorber. Photoionized O VI may be feasible in high radiation environments near AGN at observed column densities, or in extremely low column density diffuse clouds, but is largely inconsistent with the observed IGM.

In most instances of metal line absorption, we observe an apparent kinematic association of H I and O VI (typical $\Delta v \lesssim 50 \text{ km s}^{-1}$), suggesting that collisionally ionized gas and photoionized gas are spatially associated in a multiphase system, as simulations predict (Cen & Ostriker 1999; Davé et al. 2001). We assume that the two phases have the same metallicity and differ only in ionization state. Even at WHIM temperatures, there exists a small hydrogen neutral fraction ($f_{\text{HI}} \sim 10^{-6}$) and thus there should exist a hot gas signature in the Ly α profile as well as our standard WHIM

metal ions:

$$N_{\text{HI}}^{(\text{hot})} = \frac{N_{\text{OVI}}}{Z_{\text{O}}(O/H)_{\odot}} \frac{f_{\text{HI}}(T)}{f_{\text{OVI}}(T)}$$

$$= (1.5 \times 10^{13} \text{ cm}^{-2}) \left(\frac{N_{\text{OVI}}}{10^{14} \text{ cm}^{-2}} \right) \left(\frac{Z_{\text{O}}}{0.1 Z_{\odot}} \right)^{-1}. \quad (14)$$

Here, we adopt the CIE-peak ratio $f_{\text{HI}}/f_{\text{OVI}} = 7.5 \times 10^{-6}$ at $T = 10^{5.45}$ K (Sutherland & Dopita 1993) and scale N_{HI} to $N_{\text{OVI}} = 10^{14} \text{ cm}^{-2}$ and $Z_{\text{O}} = 0.1 Z_{\odot}$. Typical O VI detections are $N_{\text{OVI}} \sim 4 \times 10^{13} \text{ cm}^{-2}$, so the expected hot H I line would have $N_{\text{HI}}^{(\text{hot})} \sim 6 \times 10^{12} \text{ cm}^{-2}$ with doppler width $b_{\text{HI}} \sim 70 \text{ km s}^{-1}$, equivalent width $W_{\text{Ly}\alpha} \sim 33 \text{ m}\text{\AA}$, and a central line depth only $\sim 7\%$ below the continuum ($\tau_0 \sim 0.07$). This is marginally detectable by itself in high S/N data, but it is very difficult to separate from the stronger, narrower Ly α profile in a multiphase absorber and might be mistaken for the wings of the spectrograph point spread function. Even a strong O VI absorber ($N_{\text{OVI}} = 10^{14} \text{ cm}^{-2}$) would show $W_{\text{Ly}\alpha} = 78 \text{ m}\text{\AA}$ and a fractional depth of $\sim 15\%$ ($\tau_0 \sim 0.16$).

To investigate the existence of blended hot-plus-photoionized Ly α profiles, we compare the b_{HI} distribution of H I systems with O VI detections with those having clean O VI nondetections ($N_{\text{OVI}} < 10^{13.2} \text{ cm}^{-2}$). For the 83 systems with an O VI detection, the median and standard deviation are $b_{\text{HI}} = 31 \pm 15 \text{ km s}^{-1}$ while the 273 O VI nondetections show $b_{\text{HI}} = 26 \pm 13 \text{ km s}^{-1}$. The sample means have uncertainties of $\pm 3 \text{ km s}^{-1}$ and $\pm 2 \text{ km s}^{-1}$, respectively, which suggests that shallow, weak Ly α lines are broadening the overall H I absorption profile. Hot H I is an ideal method of tracking the WHIM and does not rely on metal enrichment. However, it is unclear whether a difference between the two populations would be apparent without the O VI diagnostic.

The O VI census in Paper 1 included only absorbers for which $W_{\text{Ly}\alpha} \geq 80 \text{ m}\text{\AA}$, yet N_{OVI} is seen to have little correlation with N_{HI} and low- N_{HI} absorbers often have comparable values of N_{OVI} in the multiphase plot. What effect does this “Ly α bias” have on the WHIM census? Weak Ly α absorbers ($W_{\text{Ly}\alpha} < 80 \text{ m}\text{\AA}$) make up 45% of our current survey, while 19 out of 83 O VI detections (23%) were seen in weak Ly α lines, which we would not have considered in Paper 1. In this survey, for the *FUSE* sample of 35 absorbers at $z < 0.15$, we find $dN/dz = 19^{+6}_{-4}$ down to 30 m \AA and $dN/dz = 60^{+38}_{-19}$ down to 10 m \AA . These compare to our finding in Paper 1, $dN/dz = 17 \pm 3$ (down to 30 m \AA) where weak H I systems were not taken into account. Our estimate, Ω_{OVI} (Table 5) is also $\sim 25\%$ higher in the low- z sample than was seen in Paper 1.

Our current survey does not fully correct for Ly α bias, since we still require an H I detection at some level to trigger a search for O VI. Tripp et al. (2008) performed an ambitious “blind” O VI survey of 16 AGN sight lines including many of those in this work. They find $dN/dz = 18.3^{+3.0}_{-2.6}$ down to 30 m \AA , compared to our $dN/dz = 15.0^{+2.7}_{-2.0}$ to the same limit ($z < 0.4$ sample). In the same sub-sample, we also find $dN/dz = 40^{+14}_{-9}$ down to 10 m \AA ($dN/dX = 54^{+12}_{-9}$). Ignoring systematic differences between the two surveys, such as our respective

criteria for absorber path length (Δz) and S/N-limited equivalent width limits, this implies that an additional $\sim 20\%$ of O VI absorbers do not have any measurable corresponding H I absorption. This effect was already apparent in a qualitative sense in the low- N_{HI} end of the multiphase plot (Figure 1b of Paper 1), where we found many absorbers with $N_{\text{OVI}} \geq N_{\text{HI}}$. When combined with the $\sim 20\%$ effect implied by the differences between this work and Paper 1 noted above, we conclude that “Ly α -bias” can have a significant effect on a complete WHIM baryon survey.

Following the example of Tumlinson & Fang (2005), we can use the O VI line frequencies, dN/dz , to constrain the distribution of metals in the low- z IGM. Referring to their Figure 2, we find that our value for the $z < 0.4$ sample, $dN/dz = 40^{+14}_{-8}$, integrated down to 10 m \AA , is consistent with a mean spatial extent of metals out to 250–300 kpc from galaxies in the Sloan Digital Sky Survey (SDSS). In this picture, and that proposed by Stocke et al. (2006b), metal enrichment occurs around dwarf galaxies of SDSS r -band absolute magnitudes down to $M_r \approx -17$ to -18 (0.03 – $0.05 L^*$).

3.1.3. C IV and N V

The ions N V and C IV are both Li-like, with strong UV resonance ($2s - 2p$) doublets. Like O VI, they may provide good WHIM tracers, at longer wavelengths accessible in the *HST* spectral band. These ions have been studied toward many Galactic high-velocity clouds (Sembach & Savage 1994; Indebetouw & Shull 2004; Sembach et al. 2003; Collins et al. 2003, 2007). However, to date, no large, low-redshift IGM surveys have been conducted in these ions. C IV is a strong absorber of an abundant element, but the STIS/E140M data are limited to $z_{\text{abs}} \lesssim 0.116$, at which redshift C IV $\lambda 1548$ shifts out of the passband. The longer wavelength STIS/E230M grating covers $0.01 < z_{\text{CIV}} < 1.0$, but this band was not often used in AGN observations.

In our new survey, we detected 24 C IV absorbers in the STIS/E140M data over a total redshift path-length $\Delta z = 2.42$ and inferred $(dN/dz)_{\text{CIV}} = 10^{+4}_{-2}$ and $\Omega_{\text{CIV}} = (7.67 \pm 1.45) \times 10^{-8}$ down to $W \geq 30 \text{ m}\text{\AA}$. At high redshift ($1.5 < z < 3.1$) Scannapieco et al. (2006) inferred $\Omega_{\text{CIV}} = 7.54 \times 10^{-8}$ with no sign of evolution over that redshift range. Similarly, Songaila (1997, 2001) inferred $\Omega_{\text{CIV}} \approx (2-7) \times 10^{-8}$ at $z = 3.0$ – 3.5 . Pettini et al. (2003) reported $\Omega_{\text{CIV}} = (4.3 \pm 2.5) \times 10^{-8}$ at $z \sim 5$ using similar column density limits as are used in this paper. The consistency of our low- z measurement to those in the early universe implies little or no evolution in C IV since reionization. This may imply a changing metal enrichment rate and/or changing ionizing flux with redshift. However, since the ionization corrections depend on both photon flux and gas density, further speculation is beyond the scope of this paper. For carbon metallicity $Z_{\text{C}} = 0.1 Z_{\odot}$, where $(\text{C}/\text{H})_{\odot} = 2.45 \times 10^{-4}$, and $f_{\text{CIV}} \approx 0.29$, the maximum ion fraction at $\log T_{\text{max}} = 5.0$ in CIE, Ω_{CIV} corresponds to a total baryon fraction associated with C IV of $\Omega_{\text{IGM}}^{(\text{CIV})} = (2.6 \pm 0.5) \times 10^{-3}$ or 25–30% that seen with O VI.

As with O VI and H I, the C IV absorbers follow a power-law distribution in column density with $\beta_{\text{CIV}} = 1.79 \pm 0.17$ (Figure 5c,d), consistent with litera-

ture values at high redshift, $\beta_{\text{CIV}} = 1.5 - 1.8$ (Songaila 1997, 2001; Ellison et al. 2000). This slope is shallower than is seen in O VI and more consistent with those of lower-ionization species. However, the uncertainty on β_{CIV} precludes any definite conclusions as to whether C IV exhibits a steep, WHIM-like distribution in column density, or a more moderate, H I-like distribution. The ionization energy required to produce C IV is only 3.52 ryd (vs. 8.37 ryd to produce O VI), thus C IV may be produced partly by photoionization by AGN and hot stars at low z (Giroux & Shull 1997). On the other hand, we see little correlation between N_{CIV} and the column densities of lower ions, even C III (see below). In contrast, there is some degree of $N_{\text{CIV}}-N_{\text{OVI}}$ correlation, suggesting that C IV may primarily trace shock-heated material. The baryon fraction traced by C IV is less than half that of O VI for a given equivalent width limit, consistent with the solar abundance ratio, $(\text{C/O})_{\odot} = 0.50 \pm 0.07$ (Allende Prieto et al. 2002; Asplund et al. 2005), and the implied sub-solar (C/O) ratio seen in the IGM (Paper 2). In the pure thermal (collisional ionization) interpretation of C IV, the cooler portions of WHIM (at $T \sim 10^5$ K) may contain a smaller portion of the baryons than at $T \sim 10^{5.5}$ K, consistent with more efficient cooling at temperatures near or below the peak of the cooling curve.

The rest wavelengths of the N V doublet (1238.821, 1242.804 Å) are well placed in the STIS/E140M data for redshift coverage out to $z_{\text{abs}} \approx 0.4$. However, the solar abundance of nitrogen is less than 20% that of oxygen. Moreover, nitrogen is a product of secondary nucleosynthesis, and its abundance relative to C and O is observed to be sub-solar in Galactic HVCs (Gibson et al. 2001; Collins et al. 2003, 2007). We detected 24 N V absorbers in one or both lines of the doublet (Figure 5e,f) over a total pathlength $\Delta z = 5.30$. Because of the lower relative abundance of nitrogen compared to carbon or oxygen, the detections are never strong, and we derive $dN/dz = 2 \pm 1$ down to 30 mÅ. Weaker N V lines are more numerous, and our total sample has $dN/dz = 7_{-2}^{+3}$ down to 10 mÅ. We detected N V and O VI together in 11 systems, and their column densities are well correlated. The ionization potential to produce N V is 5.69 ryd, and its peak CIE ion abundance occurs at $\log T_{\text{max}} = 5.25$, near to that ($\log T_{\text{max}} = 5.45$) for O VI (Sutherland & Dopita 1993). We also note that these high ions are not necessarily in equilibrium, and non-equilibrium ionization effects may alter f_{ion} . We infer a value of $\Omega_{\text{IGM}}^{(\text{NV})}/\Omega_b$ intermediate between those of O VI and C IV at both 30 and 10 mÅ (Table 12). We conclude that N V is a reliable tracer of WHIM gas based on its correlation with O VI and steep power-law slope, although with sizable error bars. Future studies of these ions with the *Cosmic Origins Spectrograph* on *Hubble* have great promise, not only to trace the WHIM but to derive nucleosynthetic signatures from a range of heavy elements (e.g., C, N, O, Si, Fe).

3.1.4. C III

We made 39 C III detections, yielding $dN/dz = 10_{-2}^{+3}$ ($dN/dX = 12_{-2}^{+4}$) down to 30 mÅ. The column density distribution shows a power-law slope of $\beta_{\text{CIII}} = 1.79 \pm 0.10$ (Figures 7a,b). Absorber frequency is com-

patible with that found in Paper 2, but spectral slope appears higher by ~ 0.2 dex. A subsample of absorbers at $z_{\text{abs}} < 0.21$, comparable to the sample used in Paper 2, shows 28 absorbers with a somewhat higher absorber frequency, $dN/dz = 14_{-3}^{+5}$ ($dN/dX = 14_{-4}^{+7}$), and a steeper column density distribution, $\beta_{\text{CIII}} = 2.06 \pm 0.15$. The reason for this discrepancy may be related to our inclusion of weaker Ly α systems, which were not studied in our previous work. Since much of the C III is expected to arise in the same photoionized gas traced by H I, we would expect that the inclusion of weaker H I systems in the survey would produce a larger number of C III systems as well. However, this does not explain the steepening of the column-density distribution seen in the low- z subsample.

In Paper 2, we saw a reasonably strong correlation between N_{HI} and N_{CIII} . The multiphase ratio was fitted with a line of slope $\alpha_{14} = 0.73 \pm 0.08$ and scale factor $C_{14} = 1.06 \pm 0.04$. From this, we incorrectly derived a metallicity for intergalactic carbon of $Z_{\text{C}} = 0.12 Z_{\odot}$, in good agreement with $Z_{\text{O}} = 0.09 Z_{\odot}$ derived in Paper 1. The *correct* derivation was lower by a factor of ten and should read $Z_{\text{C}} = 0.012 Z_{\odot}$, for a peak CIE ionization fraction $f_{\text{CIII}} = 0.83$. This inferred metallicity would increase if we chose a lower value of f_{CIII} more typical of photoionized gas. While the corrected value is substantially different from the derived oxygen metallicity in the IGM, the implied abundance ratio, $(\text{C/O})_{\text{IGM}} \sim 0.1 (\text{C/O})_{\odot}$, is compatible with the observed C III/O VI ratio (see § 4.4 and Figure 11 of Paper 2). With more C IV data, we could use both ions, C III and C IV, as a joint constraint on ionization corrections and carbon abundance.

The behavior of C III in our new study is consistent with the (corrected) previous results in Paper 2. The correlation of N_{HI} and N_{CIII} is still strong, and metallicity implied by the multiphase fit ($Z_{\text{C}}/Z_{\odot} \approx 1.5\%$) is similar to previous results for both the full sample of 39 absorbers and the 28-absorber low- z subsample. When adjusted for the mean absorber redshift of each sample and corrected by a range of ionization fractions, $f_{\text{CIII}} = 0.2-0.8$, for either photoionization or collisional ionization equilibrium, these values imply $Z_{\text{C}} = (0.015 \pm 0.002) Z_{\odot} (f_{\text{CIII}}/0.83)^{-1}$ or $Z_{\text{C}}/Z_{\odot} = 1.5 - 6\%$.

3.1.5. Si III, Si IV, and Fe III

Intergalactic Si III, Si IV, and Fe III at low redshift have received little or no attention. Along with C III discussed above, all three ions are presumed to trace primarily metal-enriched, photoionized material. All have peak CIE temperatures below 10^5 K and ionization potentials > 3 ryd. The cooling times at these temperatures are relatively short, and even at the low densities typical in the IGM, any collisionally heated material at $T < 10^5$ K should quickly cool. Such transient situations are likely places for non-equilibrium ionization effects.

Because Si III $\lambda 1206.500$ is a very strong transition, STIS observations are sensitive to extremely low column densities. Despite the lower abundance of silicon relative to more common metals ($[\text{Si/O}]_{\odot} \sim -1.4$), Si III is expected to be the dominant ionization stage in the photoionized or collisionally ionized IGM over a broad range of temperatures and photon energies. We therefore expect it to be an effective tracer of IGM enrichment,

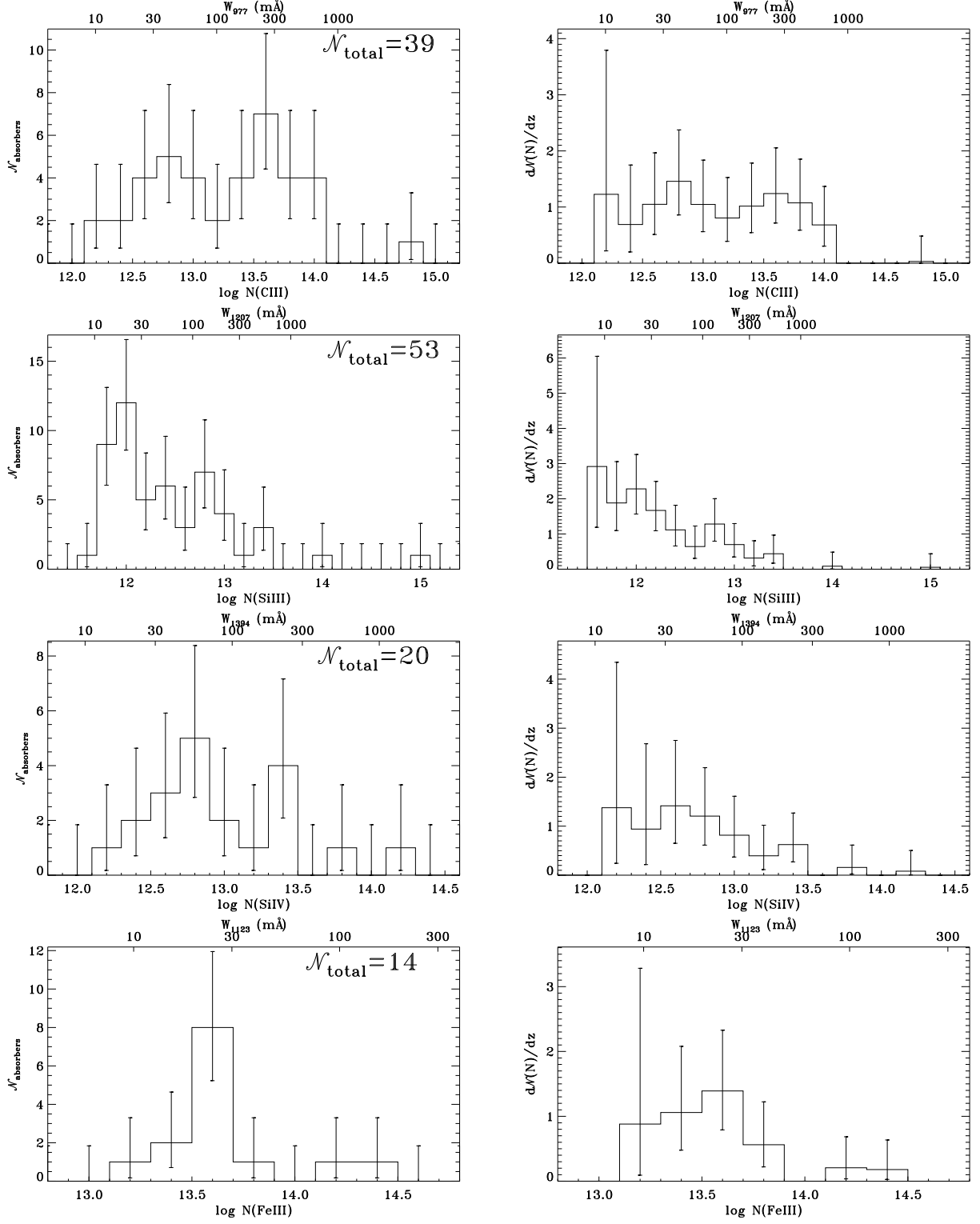


FIG. 7.— Same as Figure 5 for C III (top), Si III (second row), Si IV (third row), and Fe III (bottom).

complementary to C III or O VI. We detect Si III in 53 systems (Figures 7c,d) for $dN/dz = 6_{-1}^{+2}$ ($dN/dX = 7_{-1}^{+2}$) down to 30 mÅ or $dN/dz = 14_{-2}^{+3}$ ($dN/dX = 16_{-2}^{+4}$) down to 10 mÅ, about 40% of the value for O VI at either limit. The column-density distribution, ($d^2N/dz dN_{\text{SiIII}}$), follows a clear power law with $\beta_{\text{SiIV}} = 1.80 \pm 0.09$, consistent with β_{CIII} and β_{CIV} , slightly higher than β_{HI} .

We made 20 Si IV detections and derived $dN/dz = 4_{-1}^{+2}$ ($dN/dX = 5_{-1}^{+2}$) down to 30 mÅ (Figures 7e,f). The column density N_{SiIV} does not show a particular correlation with N_{HI} , as do N_{CIII} and N_{SiIII} . The column density distribution follows a rough power law and a fit to the cumulative distribution gives $\beta_{\text{SiIV}} = 1.92 \pm 0.17$, higher than other low-ionization species. We measure $\Omega_{\text{SiIV}} = (8.3 \pm 1.3) \times 10^{-8}$ down to 30 mÅ. For absorbers at high redshift, Scannapieco et al. (2006) measured $\Omega_{\text{SiIV}} = 6.0 \times 10^{-9}$ to $\log N_{\text{SiIV}} > 12$ at $\langle z \rangle = 2.4$, a factor of 14 lower than our most sensitive limit at $\langle z \rangle \sim 0.1$. They see no evidence for evolution in Si IV in the redshift range $1.5 < z < 3.1$. Similarly, Songaila (1997, 2001) measured $\Omega_{\text{SiIV}} = (7 - 30) \times 10^{-9}$ at $1.5 < z < 5.5$. This factor of 2.5 – 12 increase in the Si IV fraction between the early and modern universe is opposite to the behavior of C IV above, which remains essentially unchanged. This may imply some combination of changes in the metagalactic ionization field and/or IGM enrichment.

Fe III is a relatively weak transition ($f = 0.0544$, Morton 2003) of a relatively low-abundance element ($[\text{Fe}/\text{O}]_{\odot} \approx -1.4$) and thus it comes as no surprise that we make only 14 detections (Figure 7g,h) with $dN/dz \sim 1$ down to 30 mÅ. The power-law slope is the steepest of any in our survey ($\beta_{\text{FeIII}} = 2.2 \pm 0.4$) but with such large uncertainty as to render any comparison speculative. As with N_{OVI} , N_{FeIII} shows only cursory correlation with N_{HI} and covers a range of 1.5 dex in column density, while N_{HI} is seen over almost three decades. This evidence is exactly what we used in Paper 1 to argue that O VI and H I were tracing different IGM phases. However, given the low ionization energy required to produce Fe III (16.18 eV), it is likely that Fe III and H I arise in similar photoionized gas. We may be seeing preferential iron enrichment in material that has been shocked and cooled to ambient temperatures. We will return to these issues and their redshift dependence in a future paper that deals with IGM absorber evolution.

3.2. Ion Ratios and Comparison with Models

With such a rich data set, many absorbers show detections in more than one ion, allowing us to compare observed line ratios with predictions from a set of simple CLOUDY models. In Paper 2 we compared the observed C III/O VI ratios for 13 absorbers with models and concluded that a single thermal-plus-photoionized phase could not realistically account for the observations. We found that C III and O VI absorbers probably included both photoionized and collisionally ionized gas, although O VI was likely to be mostly collisionally ionized.

In this work, we use the same set of models: a four-dimensional grid calculated using CLOUDY v96.01 with parameters temperature T , ionization parameter

U , metallicity Z (relative to solar values), and hydrogen number density n (cm^{-3}). We simulate the effects of collisional ionization by setting the cloud to a constant temperature in each model. Low temperatures, $T \approx (1 - 3) \times 10^4$ K, approximate a pure photoionization model, while low photoionization parameters, $\log U < -4$, are equivalent to a pure CIE model. These models were calculated for a 400 kpc thick optically thin slab of gas illuminated on one side by an AGN radiation field with a power-law continuum $F_{\nu} \propto \nu^{-\alpha_s}$ in the EUV (1–4 ryd) and soft X-ray (10–22 ryd) with $\alpha_s = 1.8$ (Haardt & Madau 1996; Fardal et al. 1998; Telfer et al. 2002). Since a more realistic isotropic radiation field illuminates the slab from all sides, the actual photon density is a factor of 4 higher (+0.6 dex) than that output by the models; we have adjusted all citations to reflect this. We also computed a second grid of CLOUDY models assuming $n = 10^{-5} \text{ cm}^{-3}$, $Z = 0.1 Z_{\odot}$, and pure photoionization (no thermal ionization component), but we allowed the ionization parameter U and spectral index α_s to vary between $1 < \alpha_s < 3$ (Telfer et al. 2002; Shull et al. 2004). The equilibrium temperatures of the pure photoionization models was $\log T = 4.1 - 4.3$.

Observed Si III and Si IV show a strong correlation in column density ($R = 0.85$, $N_{\text{SiIII}} \propto N_{\text{SiIV}}^{1.0 \pm 0.1}$, Fig. 8a), suggesting that the two ions trace the same gas. Since Si III/Si IV are adjacent ionization states of the same element, we can avoid complications arising from abundance and metallicity and use $N_{\text{SiIII}}/N_{\text{SiIV}}$ as a tracer of the ionization state of the cloud. The observed ratios show some scatter, $\langle \log (N_{\text{SiIII}}/N_{\text{SiIV}}) \rangle = 0.1 \pm 0.4$, but all 12 systems in which both ions appear can be explained as a single-phase absorber, either collisionally ionized at $T = 10^{4.8 \pm 0.2}$ K or photoionized with $\log U = -1.6 \pm 0.7$. Variations in model metallicity and density do not produce significant shifts in allowed parameter space, nor does changing the photoionizing spectral index α_s significantly alter the (U, T) solution. Unfortunately, the doppler b -values for the lines are of little help in constraining the temperature solution; the median line width for these Si ions is $b \sim 30 \text{ km s}^{-1}$, corresponding to $T > 10^6$ K for a case of pure thermal broadening. We conclude from this that the low-ionization material is consistent with photoionized clouds with $\log U \sim -1.6$. Similar CLOUDY models and silicon ion ratios in Galactic high velocity clouds (HVCs) show $\log U \sim -3$, presumably due to much higher gas densities (see Collins et al. 2003, 2007; Westbrook et al. 2008).

C III and C IV are the other pair of adjacent ions in this work. Detections in both species occur in only eight absorbers (Figure 8b), and the column densities are not well correlated ($R \sim 0.5$). Still, the detections are consistent with a 1:1 column-density ratio, and the absolute scatter in $\log (N_{\text{CIII}}/N_{\text{CIV}})$ is actually smaller than for $\log (N_{\text{SiIII}}/N_{\text{SiIV}})$. Compared to the models, the range of observed $N_{\text{CIII}}/N_{\text{CIV}}$ is consistent with either $\log U = -1.4 \pm 0.5$ or $\log T = 5.0 \pm 0.1$, near the peak CIE fractional abundance of C IV. However, since N_{CIV} and N_{CIII} do not show the same degree of correlation present in the Si ions and since we believe C IV to be collisionally ionized in at least some cases, we hesitate to assign too much significance to the C III/C IV model comparisons.

Because of the expected redshift evolution of the

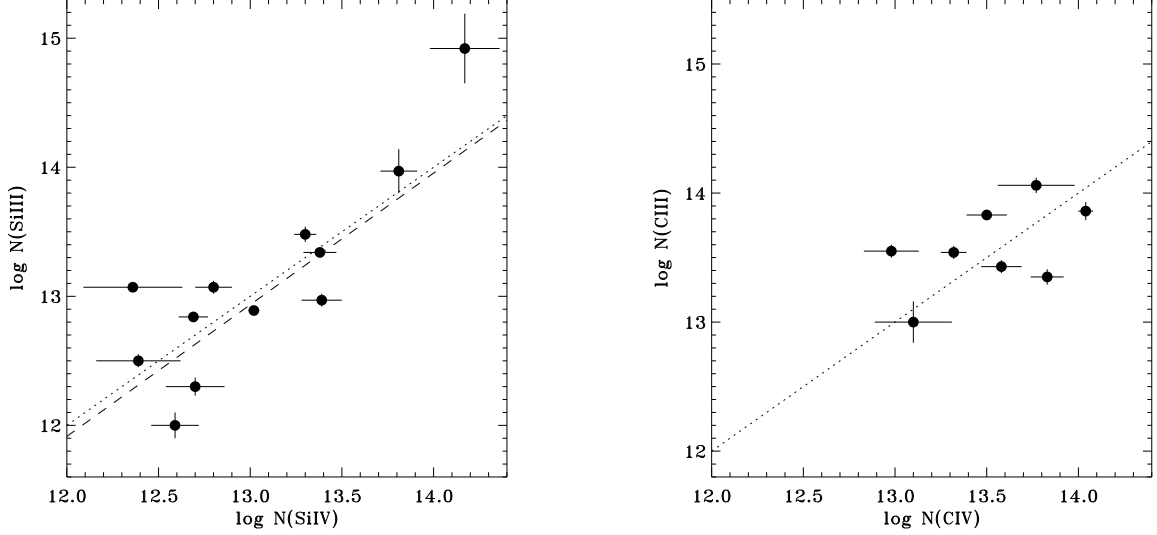


FIG. 8.— Detections of both Si III and Si IV (left) and C III and C IV (right). The column densities of the Si ions are well-correlated ($R = 0.87$), and the linear fit (dashed) has a slope 1.1 ± 0.1 , consistent with a 1:1 ratio (dotted). The correlation is much less for the carbon ions ($R = 0.52$), although the data are also consistent with a 1:1 ratio (dotted). The absolute scatter for each pair of ions is similar.

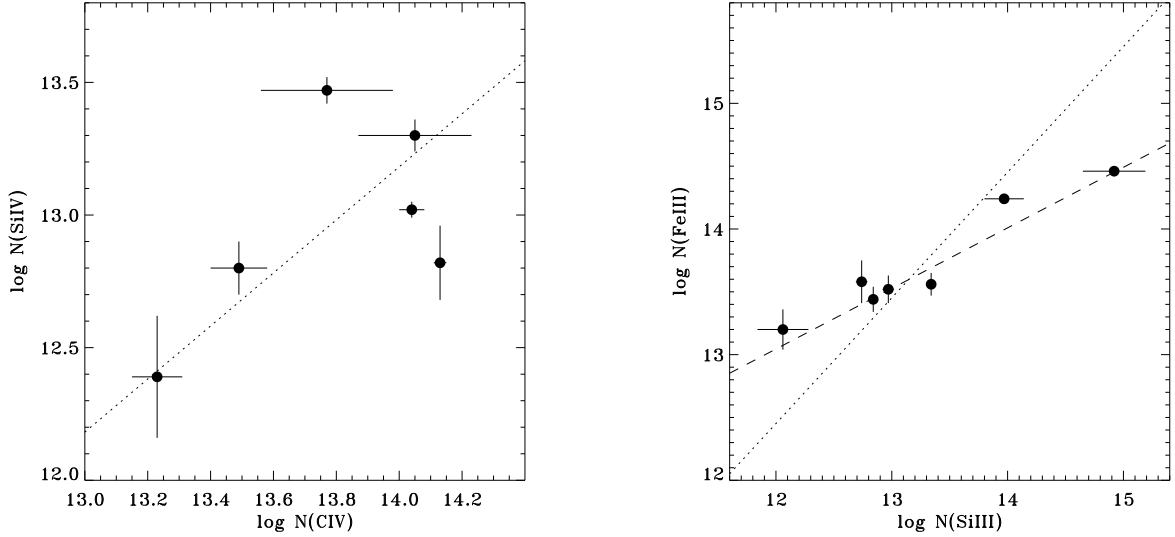


FIG. 9.— Line ratio plots for the same ionization stages of different elements. Six absorbers with both C IV and Si IV detections show some correlation (left), but the general trend is consistent with $N_{\text{CIV}} \propto N_{\text{SiIV}}$ (dotted). Si III and Fe III (right) appear in seven absorbers and are extremely well-correlated over several decades, but with $N_{\text{FeIII}} \propto N_{\text{SiIII}}^{0.5 \pm 0.1}$ (dashed), not 1:1 proportionality (dotted).

thermal state, ionization state, and metallicity of the IGM, it is useful to compare our low- z results with those seen in the early universe. High redshift ($z > 2$) Si IV is often compared to C IV as a probe of the metagalactic ionizing background (Songaila 1998; Kim, Cristiani, & D’Odorico 2002; Scannapieco et al. 2006), or as a measure of the α -process versus RGB stellar nucleosynthesis (McWilliam 1997), however both analyses assume that both ions are photoionized. For young nucleosynthetic systems, one expects to observe abundance enhancements in α -process elements (Si, O) relative to (C, Fe). However, deriving accurate (Si/O) and (Si/C) abundances is difficult, owing to the dependence of ionization corrections on the shape of the ionizing spectra (Giroux & Shull 1997). We see six ab-

sorbers with both Si IV and C IV detections with $-1.3 \leq \log(N_{\text{SiIV}}/N_{\text{CIV}}) \leq -0.3$, similar to the range seen at higher redshift. The correlation is moderate ($R = 0.6$), but the general trend is consistent with a linear relationship between the two species (Figure 9a).

The ion pairs Fe III/Si III and C III/Si IV have similar ionization potentials and thus their column density ratios should be relatively insensitive to the ionizing spectrum. These two pairs provide probes of relative C/O/Si/Fe abundance ratios in the IGM. C III and Si IV are seen together in six absorbers and are poorly correlated. However, the observed $\langle \log(N_{\text{CIII}}/N_{\text{SiIV}}) \rangle = 0.7 \pm 0.6$ is slightly lower than model predictions at $\log U \approx -1.5$, suggesting, if the single-phase assumption is used, an overabundance of silicon/carbon by ~ 0.3 dex with re-

spect to solar values.

Fe III and Si III are seen together in 7 systems and their column densities are well-correlated ($R > 0.9$) though with $N_{\text{FeIII}} \propto N_{\text{SiIII}}^{0.5 \pm 0.1}$ (Fig. 9b). The modeled $N_{\text{FeIII}}/N_{\text{SiIII}}$ values depend on U , but for $\log U \approx -1.5$ and solar $[\text{Fe}/\text{Si}]$, the observed values, $\langle \log(N_{\text{FeIII}}/N_{\text{SiIII}}) \rangle = 0.5 \pm 0.5$, are too high by a factor of 2-3 dex. If Fe III and Si III truly arise in the same gas, normal photoionization corrections require an enormous overabundance of iron in the IGM, $[\text{Fe}/\text{Si}]_{\text{IGM}} = 2.6 \pm 1.2$. A similar iron overabundance is found by comparing Fe III/C III.

The basic issue here arises because of the low ionization threshold (30.63 eV) and high cross section for photoionizing Fe III to Fe IV. If Fe/Si and Fe/C are in solar abundance ratios, it is difficult to obtain $N_{\text{FeIII}} > N_{\text{SiIII}}$. In many of the IGM absorbers detected in both ions (Fig. 9b), the observed column density ratio is $[\text{Fe III}/\text{Si III}] = 0.5 \pm 0.3$, whereas CLOUDY models predict much lower ratios. The solution to the Fe III problem may lie in details of the assumed AGN spectrum; we use a continuous power-law spectrum from 1-22 ryd, which leads to Fe III being photoionized to Fe IV. A power law with a slope break at 3-5 ryd, as proposed by Haardt & Madau (2001), results in relatively less flux at higher energies and boosts the predicted Fe III columns. However, this would make the production of photoionized C IV and other high ions even more difficult. With more data and a larger survey, we might be able to distinguish among several competing effects: metallicity enhancements of $[\text{Fe}/\text{Si}]$ due to nucleosynthesis, changes in the ionizing radiation field changes around 3-5 ryd, and the relative portions of Fe III, Si III, and C III in various ionization phases.

The CLOUDY models can also be applied to the high ions, believed to reside in the WHIM. The correlation is much better for the eleven systems with both N V and O VI absorption ($R = 0.8$, Fig. 10a). The observed best fit has a slope of 0.75 ± 0.08 , but a fit with slope of 1 is quite plausible with an offset of -0.74 ± 0.03 dex, comparable to the solar abundance, $\log(N/O)_{\odot} \sim -0.7$. Unfortunately, these three ions are neither of the same element nor do they have overlapping ionization potentials, so there is an abundance/ionization degeneracy in the (U, T) solutions. Assuming a solar N/O abundance, we find that the observations are consistent with collisionally ionized systems at $T = 10^{5.35 \pm 0.10}$ K, midway between the peak CIE abundance temperatures of the two ions. Changing the N/O abundance to the sub-solar values typically seen in HVC gas (Gibson et al. 2000, 2001; Collins et al. 2003, 2007) does not change the temperature solution appreciably.

Observed N V/O VI ratios are also consistent with pure photoionization models with $\log U = -0.4 \pm 0.5$. However, this is a factor of ~ 10 higher than that derived from the low ion ratios. This pattern is familiar from the O VI/C III results in Paper 2, where C III suggested $\log U \sim -1.5$, while photoionized O VI required $\log U \sim -0.5$. Altering the relative N/O abundance in the IGM varies the ionization parameter solution. Matching the observed ratios to the derived $\log U = -1.5$ requires a relative N/O overabundance of 0.3-1.3 dex, opposite to the trend observed in HVCs. Varying the slope

of the ionizing spectrum will also alter the predicted ratio, but an extremely hard incident spectrum ($\alpha_s < 1$) is required for a $\log U = -1.5$ solution. Based on observations of nearby AGN, a spectral slope this steep is deemed unrealistic.

C IV and O VI appear together in eleven systems though the correlation is not as clear as with N V vs. O VI ($R = 0.6$, Fig. 10b). The best fit slope is 0.7 ± 0.1 though a 1:1 fit with an offset of -0.64 ± 0.04 is plausible. This offset may be a manifestation of the sub-solar C/O ratio implied in Paper 2, or it may reflect the faster cooling times experienced by lower temperature shocked gases.

The model (U, T) solution is similar to that for N V/O VI above; $\log U \sim -0.5$ or $T \sim 10^{5.4 \pm 0.1}$ K for a solar C/O ratio. Again, matching observed C/O to a $\log U \sim -1.5$ solution requires C to be overabundant with respect to O by ~ 0.6 dex, opposite the subsolar C/O ratio implied in Paper 2.

3.3. WHIM Cosmology and Metallicity of the IGM

Integrated down to the lowest level of detectable absorbers ($W \sim 10$ mÅ), our survey of three high metal ions estimates that they trace baryon contents of approximately $\Omega_{\text{IGM}}^{(\text{ion})} \approx 9\%$ (O VI), 5% (N V), and 3% (C IV) of the total. These estimates scale inversely with an assumed IGM metallicity of 10% solar and the adopted ionization corrections characteristic of maximum abundance in CIE: $f_{\text{ion}} = 0.22$ (O VI), 0.24 (N V), and 0.29 (C IV). We see that the WHIM baryon fraction, $\Omega_{\text{IGM}}^{(\text{ion})}$, implied by O VI absorption is greater than that from N V, which in turn is greater than that from C IV. However, these differences should not be taken too seriously, since there are many assumptions that go into these estimates. First, the ionization fractions may differ from CIE, particularly if photoionization plays some role in the C IV absorbers. Second, these ions have different sensitivity limits in column density owing to line strengths and their location at different wavelengths. Alternatively, the differences may represent a true gradient in Ω_{WHIM} as a function of temperature. The latter interpretation is plausible since O VI, N V, and C IV have peak CIE temperatures of 3, 2, and 1×10^5 K, respectively, and radiative cooling rates have a steep dependence on temperature in that regime (Sutherland & Dopita 1993). Given its poor correlation with O VI and N V, many C IV absorbers may be photoionized gas rather than thermal in nature. Thus, $\Omega_{\text{WHIM}}^{(\text{CIV})}$ should probably be taken as an upper limit until we can refine the multiphase nature of the absorbers with additional data from larger C III and C IV surveys.

At our most sensitive O VI limit ($W > 10$ mÅ), we find $\Omega_{\text{WHIM}} = 8.6 \pm 0.8\%$. This is higher than the value quoted in Paper 1 ($\sim 5\%$), probably because we now include weaker Ly α systems (the Ly α -bias) and have better statistics in the weak O VI absorbers themselves. However, the power-law slope of the WHIM ions is steep, with a similar amount of mass in the numerous weak absorbers as in the infrequent strong absorbers. Future WHIM surveys sensitive to lower N_{OVI} limits may well increase the baryon mass fraction in the WHIM closer to the 30-50% predicted by simulations (Davé et al. 1999; Cen & Fang 2006).

X-ray probes of the WHIM at $T > 10^6$ K, where

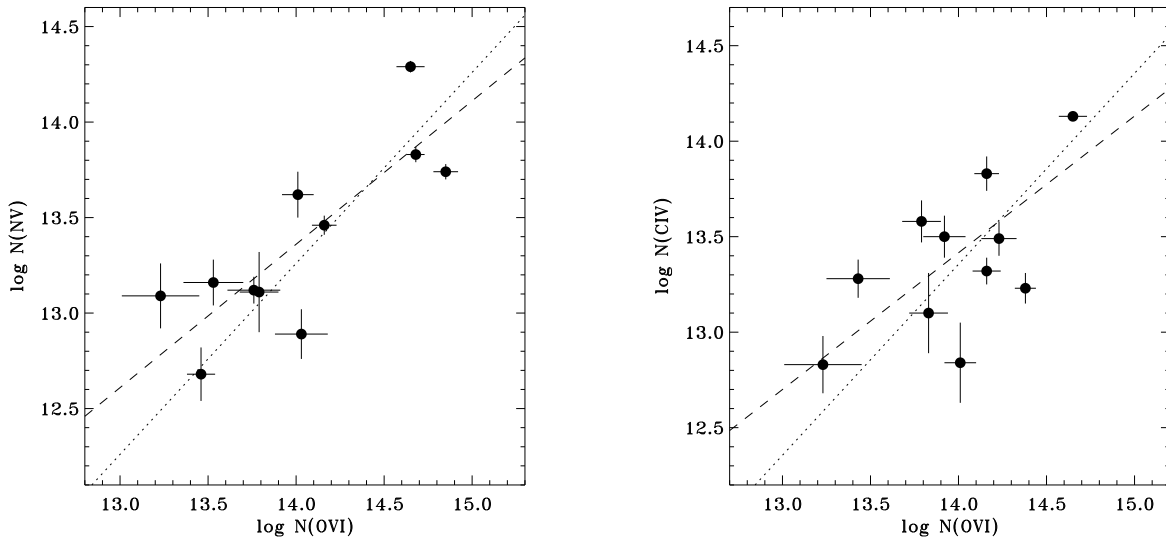


FIG. 10.— Correlations between highly ionized species. The column densities of NV and O VI (left) are well correlated in eleven absorbers ($R = 0.81$), and the best fit (dashed) has a slope of 0.75 ± 0.08 . However, a 1:1 fit is plausible (dotted), with an offset of -0.74 ± 0.03 dex, consistent with $\log (N/O)_{\odot} \approx -0.7$. CIV and O VI appear together in eleven absorbers (right), but the correlation is only moderate ($R = 0.62$). Much like NV vs. O VI, the best fit slope is ~ 0.7 (dashed) but the data are consistent with a 1:1 relationship with an offset of ~ -0.6 (dotted).

a considerable fraction of WHIM is predicted to exist, are not yet available with the same fidelity as FUV WHIM tracers (O VI, etc). For example, O VII $\lambda 21.60$ is 9.1 times weaker ($f\lambda$) and O VIII $\lambda 18.97$ is 17.4 times weaker than O VI $\lambda 1032$. Partially offsetting these atomic ratios are the CIE peak ionization fractions of O VII and O VIII, which are 3–4 times that of O VI. However, the primary contribution to the low X-ray spectral sensitivity comes from the low resolution of the grating spectrographs aboard *Chandra* (700 km s $^{-1}$ at 20 Å) and *XMM-Newton* (~ 1000 km s $^{-1}$), compared to those on *Hubble* (7–20 km s $^{-1}$) or *FUSE* (20 km s $^{-1}$). Thus, the O VI surveys probe hot gas down to $N_{\text{OVI}} \approx 10^{13}$ cm $^{-2}$, whereas the recent claimed O VII and O VIII detections are at the level $N_{\text{OVIII}} \approx 5 \times 10^{15}$ cm $^{-2}$ (toward PKS 2155–304, Fang et al. 2002; Fang, Canizares, & Yao 2007) and $N_{\text{OVII}} \approx 1 \times 10^{15}$ cm $^{-2}$ (toward Mrk 421, Nicastro et al. 2005) with significant uncertainties. However, these redshifted IGM absorbers have not been seen in *XMM/Newton* observations (Rasmussen et al. 2007; Kaastra et al. 2006) and their verification is therefore in doubt (Bregman 2007). Thus, for the moment, the X-ray detection statistics of remain highly uncertain while FUV spectroscopy provides our best (only?) measurements of the WHIM, limited to the regime with $T < 10^6$ K.

In the photoionized H I gas in the Ly α forest, Penton, Stocke, & Shull (2004) found that $29 \pm 4\%$ of the local baryon mass could be accounted for down to $\log N_{\text{HI}} = 12.5$ ($W_{\text{Ly}\alpha} = 17$ mÅ). We determine values of Ω for H I via equations 9 and 10 and present the results in Table 13 and Figure 11 for different $\log N_{\text{HI}}$ values. Our survey of 650 Ly α absorbers gives $\Omega_{\text{IGM}}^{(\text{HI})}/\Omega_b = 29 \pm 4\%$ integrated down to the same column density limit as Penton et al. but with ~ 3 times higher pathlength Δz . Both results are consistent with cosmological simulations, which find that $\Omega_{\text{IGM}}^{(\text{HI})}/\Omega_b = 20 - 40\%$ (Davé et al.

1999, 2001; Cen & Ostriker 1999; Cen & Fang 2006).

Low ions such as C III and Si III likely trace the subset of the Ly α forest that is enriched by star formation and galaxy feedback. Using these ions as probes of metallicity will allow us to look for evolution of metallicity with z and N_{HI} . We can also look for patterns indicative of nucleosynthesis near galaxies and effects on ion state arising from multiphase photoionized and collisionally ionized gas. In the doubly-ionized species, we see $\Omega_{\text{IGM}}^{(\text{ion})}/\Omega_b = 1 - 4\%$ (Table 12), well below the $\sim 30\%$ value for the Ly α forest as a whole if we take the fiducial CIE values for f_{ion} listed in Table 3. The assumed ion fractions for C III, Si III, and Fe III are

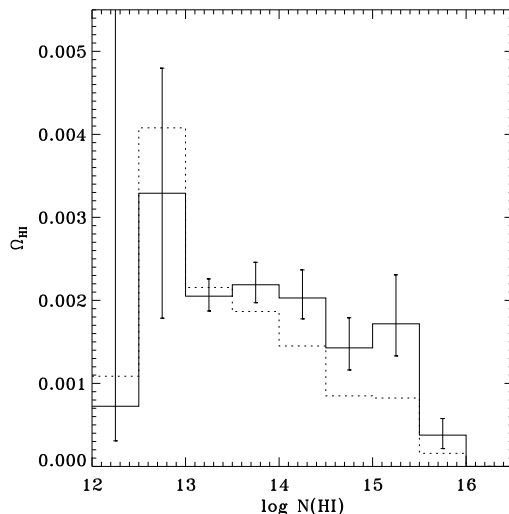


FIG. 11.— Differential Ω_{HI} as a function of $\log N_{\text{HI}}$ for 650 Ly α absorbers calculated by the methods of Penton et al. (2000, solid) and Schaye (2001, dotted). The $\log N < 12.5$ bin contains only 17 absorbers and is not included in our calculations of cumulative Ω_{HI} in Table 13.

TABLE 13
BARYON CONTENT OF THE LOCAL $\text{Ly}\alpha$ FOREST

log N_{HI} Range	\mathcal{N}	$\Omega_{\text{Ly}\alpha}^{\text{a}}$	$\Omega_{\text{Ly}\alpha}/\Omega_b$ (%) ^a	$\Omega_{\text{Ly}\alpha}^{\text{b}}$	$\Omega_{\text{Ly}\alpha}/\Omega_b$ (%) ^b
12.5 – 13.5	373	0.0053 ± 0.0015	11.7 ± 3.3	0.0062 ± 0.0019	13.7 ± 4.1
13.5 – 14.5	206	0.0042 ± 0.0004	9.3 ± 0.8	0.0033 ± 0.0003	7.3 ± 0.7
14.5 – 15.5	50	0.0031 ± 0.0006	6.9 ± 1.3	0.0017 ± 0.0003	3.7 ± 0.7
15.5 – 16.5	4	0.0004 ± 0.0002	0.8 ± 0.4	0.0002 ± 0.0001	0.3 ± 0.2
12.5 – 14.5	579	0.0096 ± 0.0016	21.0 ± 3.4	0.0096 ± 0.0019	21.0 ± 4.2
14.5 – 16.5	54	0.0035 ± 0.0006	7.7 ± 1.4	0.0018 ± 0.0003	4.0 ± 0.7
12.5 – 16.5	633	0.0131 ± 0.0017	28.7 ± 3.7	0.0114 ± 0.0019	25.0 ± 4.2

^a Method of Penton, Shull, & Stocke (2000) ^b Method of Schaye (2001)

all close to unity. Lower values of f_{ion} , as might be the case in non-equilibrium ionization, would produce smaller baryon fractions and we conclude that $\Omega_{\text{IGM}}^{(\text{ion})}$ is an upper limit in the case of the doubly-ionized species. Likewise, the baryon fraction probed by Si IV at low z is surprisingly high, $\Omega_{\text{IGM}}^{(\text{SiIV})}/\Omega_b = 8 \pm 1\%$, comparable to that of O VI. However, Si IV is most likely photoionized, and thus the CIE ion fraction $f_{\text{SiIV}} \sim 0.2$ assumed in this calculation may be too low. These two limits suggest $1\% \lesssim (\Omega_{\text{IGM}}^{(\text{ion})}/\Omega_b) \lesssim 8\%$, or that roughly 3-25% of the local $\text{Ly}\alpha$ forest by mass is enriched at a currently detectable level. More sophisticated models may shed light on this problem.

As in Papers 1 and 2, we estimate the metallicity of IGM material based on multiphase ratios (Table 11). The values generated cover a wide range from $Z_{\text{Fe}} = 0.7 Z_{\odot}$ to $Z_{\text{CIII}} = 0.015 Z_{\odot}$. With Z_{OVI} and Z_{CIII} we reproduce the result, $[\text{C/O}] \approx 0.1 [\text{C/O}]_{\odot}$, reported in Paper 2, however, C IV reports $Z_{\text{C}} = 0.055$, a factor of 3 higher than estimated by C III. Similarly, adjacent Si ions disagree on IGM Si abundance by a factor of eight. As with $\Omega_{\text{IGM}}^{(\text{ion})}$ above, each metallicity estimate scales as $[f_{\text{ion}}]^{-1}$, so that the inferred metallicities for the low ions may be upper limits. However, this puts the adjacent-ion metallicity estimates even further from agreement. With larger data bases, it may be better to perform a joint analysis of ion pairs such as C III/C IV and Si III/Si IV, to arrive at consistent values for $\log U$ and Z .

If we restrict ourselves to species with the most detections (O VI, C III, Si III) we see that the WHIM tracer (O VI) shows $Z \approx 0.15 Z_{\odot}$ while the $\text{Ly}\alpha$ forest tracers (C III, Si III) have a lower metallicity ($Z \sim 0.02 Z_{\odot}$). The pattern can be forced a bit by including C IV ($Z \sim 0.05 Z_{\odot}$). This would imply that shocked material traced by high ions tends to have somewhat higher metallicity than the ambient IGM, as one would expect if both shocks and enrichment were products of galactic winds and star formation feedback. However, N V, Si IV, and Fe III break the metallicity-ionization potential pattern with anomalously high values. Future nearest-neighbor-galaxy studies (e.g., Prochaska et al. 2006; Stocke et al. 2006b) may help make sense of these confusing multiphase ratio metallicity estimates. In particular, nucleosynthetic effects may show up in galactic outflows which may be partially responsible for IGM shock heating traced by O VI.

4. CONCLUSIONS AND SUMMARY

We present the results of the largest low-redshift IGM survey to date. In total, we analyzed 650 H I absorbers at $z < 0.4$ along 28 AGN sight lines. For each IGM system, we measured detections or upper limits in 13 transitions of 7 metal ions as well as H I ($\text{Ly}\alpha$, $\text{Ly}\beta$, O VI, N V, C IV, C III, Si IV, Si III, and Fe III).

Our O VI results reinforce Danforth & Shull (2005) results but over a broader redshift range, and to a slightly deeper sensitivity limit. We found 40 O VI absorbers in Paper 1 at $z < 0.15$ and expand the sample to 83 O VI absorbers at $z < 0.4$ in this work. The dN/dz turnover below $\log N_{\text{OVI}} = 13.4$ seen in Paper 1 is not reproduced in the larger dataset, at least down to $\log N_{\text{OVI}} = 13.0$. Detection statistics from the low- z bin of this survey are consistent with equivalent values from Paper 1. Comparison of dN/dz , α_{14} , and Ω between high and low redshift bins hits at z -evolution in dN/dz , α_{14} , and derivative quantities.

The N V detections are not as common as O VI (24 vs. 83) owing to the lower cosmic abundance of nitrogen. However, N V shows excellent correlation with O VI in column density and displays many of the same characteristics (steep power-law slope, lack of correlation with H I) and we conclude that N V is a reliable tracer of WHIM material. C IV is a strong transition of an abundant metal, but our detection statistics are hampered by the limited redshift range in which we can observe ($z < 0.112$). Nevertheless, N_{CIV} does not appear to be well-correlated with either WHIM tracers (O VI, N V) nor lower ions (C III, H I) and thus may arise from both photoionization and shocks. We conclude that C IV is not a conclusive WHIM tracer, though it is a good probe of metal enrichment. Longer wavelength observations of AGN sight lines would improve the statistics of this ion.

We made numerous detections of both C III and Si III in IGM absorbers (39 and 53, respectively). Column densities of both ions show reasonable correlation with N_{HI} , and the dN/dz distributions are similar, leading us to classify both ions as predominantly photoionized.

Detections of both Si IV and Fe III are not as plentiful as the other low ions, and conclusions are harder to reach. Still, the majority of the Si IV detections (12/20) also show Si III absorption, and N_{SiIII} and N_{SiIV} are very well correlated. We compare our observed line ratios with a set of CLOUDY models and find them consistent with a photoionized IGM with $\log U = -1.6 \pm 0.7$. Our other adjacent ion pairs (C III/IV) appear together in only eight absorbers and their column densities are

not well-correlated. However, they are consistent with models with $\log U = -1.4 \pm 0.5$. Based on these diagnostics, we conclude that typical IGM clouds have an ionization parameter of $\log U \approx -1.5 \pm 0.5$. Photoionization models with U ten times higher would be required to explain the observed $N_{\text{NV}}/N_{\text{OVI}}$ and $N_{\text{CIV}}/N_{\text{OVI}}$ ratios, and this bolsters our interpretation of those species as collisionally ionized.

N_{FeIII} appears stronger than predicted by CLOUDY models by a factor of ~ 100 or more when compared to either N_{SiIII} or N_{CIII} . This may be indicative of a softer ionizing spectrum above ~ 3 ryd than was assumed in the models, but that explanation causes a set of other problems. More sophisticated modeling is required to explain these observations.

4.1. Status of the Baryon Census

With an unprecedented number of H I absorbers, we conclude that the Ly α forest makes up $29 \pm 4\%$ of the local baryonic material by mass. This is compatible with previous surveys (Penton, Stocke, & Shull 2004) as well as simulations (Davé et al. 1999, 2001). C III and Si III detection statistics suggest that 3-25% of the Ly α forest material is enriched with metals at a detectable level at low z .

At our most sensitive limit, $\log N_{\text{OVI}} \geq 13.0$, we can further account for $8.6 \pm 0.7\%$ of the baryons residing in the WHIM at temperatures around $T = 10^{5.5}$ K via O VI observations. Our N V detections suggest a smaller WHIM fraction, consistent with nitrogen's lower abundance and lower range of temperatures over which it is abundant. However, the dN/dz distributions of both WHIM tracers are fitted with a power law of index $\beta \approx 2$, implying that weak absorbers contribute as much to the mass fraction as strong absorbers. More sensitive FUV surveys will likely increase the WHIM fraction.

Additionally, there is the issue of "Ly α bias". In Paper 1, we examined only strong Ly α systems ($W_{\text{Ly}\alpha} > 80$ mÅ), yet N_{OVI} was shown to have little or no correlation with N_{HI} . In this work, we set out to minimize this bias by including all detected H I systems, no matter how weak. Inclusion of weaker Ly α lines in the survey boosts O VI detection statistics and all related quantities (dN/dz , $\Omega_{\text{IGM}}^{(\text{ion})}$) by $\sim 20\%$ compared with the previous survey. However, even this survey results in some Ly α bias since H I detections are required at some level, and the finite S/N of the data limits this to $W_{\text{Ly}\alpha} \gtrsim 15$ mÅ in even the best data. The results of Tripp et al. (2008) suggest an additional $\sim 20\%$ increase if O VI systems are measured with *no* corresponding H I detection. Combining these two effects, we suggest that the Ly α bias on WHIM surveys is a real effect at the level of 20-40%. Thus we suspect the true value of Ω_{WHIM} as detected

via O VI absorption is probably closer to 10% of Ω_b .

Even reliable WHIM tracers such as O VI and N V can only detect material that has been significantly enriched above primordial metallicity. Thus, there is a metallicity bias in this survey. If we take the very rough 3%-25% value from the Si III and other low ion estimates discussed above as a typical fraction of the IGM enriched to detectable levels, that may boost the true fraction of material at $T = 10^{5-6}$ K by 3-25 times ($\sim 30\% - 250\%$ of the baryons)! Clearly the latter value is unphysical, but $\Omega_{\text{WHIM}} \sim 30\%$ is plausible and consistent with some simulations.

But what about the balance of the baryon census? If condensed objects (stars, galaxies, etc) account for $\sim 7\%$ of cosmological baryons (Salucci & Persic 1999), then $\sim 50\%$ of the local baryons remain unaccounted for. Cooling of diffuse gas is fastest at lower temperatures, so it is likely that there is a vast hot reservoir of gas in the IGM (Cen & Ostriker 1999; Shull 2003). This hot WHIM ($T > 10^6$ K) is inaccessible through FUV absorption lines, and the primary metal ions (O VII, O VIII) are only detected in the X-ray. While O VII and O VIII absorption has been seen associated with the Galaxy and certain AGN (Nicastró et al. 2005; Fang, Canizares, & Yao 2007), there are no confirmed measurements of these lines in the IGM. This remains a challenge for sensitive X-ray spectrographs of the future.

The scheduled August 2008 installation of the *Cosmic Origins Spectrograph* on HST will provide a great opportunity to study the low- z IGM. With greater than ten times the sensitivity of STIS and a resolution comparable to that of *FUSE*, high resolution, high signal-to-noise observations of faint quasars will become feasible in very reasonable observing times. High throughput will enable us to observe many fainter AGN targets, many with very large pathlengths ($z < 0.45$). This will increase the available total IGM path length by perhaps an order of magnitude or more. With this increase will come a proportional boost in detection statistics of WHIM tracers such as O VI and N V as well as Ly α , Si III, C IV, and a host of other astrophysical interesting lines.

This work was supported by *FUSE* grant NNG06GI91G, and NASA Theory grant NNX07AG77G. The authors wish to acknowledge several fruitful conversations with Mark Giroux on the subject of line ratios and metagalactic ionizing radiation and John Stocke regarding cosmic variance and line identifications. We thank Steve Penton for his expertise in reducing the STIS Echelle data, Renyue Cen and Taotao Fang for supplying the data for the simulations used in Figure 6, and Gary Ferland for feedback on our CLOUDY models.

REFERENCES

- Allende Prieto, C., Lambert, D. L., & Asplund, M. 2002, ApJ, 573, L137
 Asplund, M., Grevesse, N., & Sauval, A. J. 2005, in Cosmic Abundances as Records of Stellar Evolution and Nucleosynthesis, ASP Conf. Ser. 336, 25
 Bahcall, J. N., & Peebles, P. J. E. 1969, ApJ, 156, L7
 Bregman, J. N. 2007, ARA&A, 45, 221
 Cen, R., & Fang, T. 2006, ApJ, 650, 573
 Cen, R., & Ostriker, J. P. 1999, ApJ, 519, L109
 Cen, R., & Ostriker, J. P. 2006, ApJ, 650, 560
 Collins, J. A., Shull, J. M., & Giroux, M. A. 2003, ApJ, 585, 336
 Collins, J. A., Shull, J. M., & Giroux, M. A. 2007, ApJ, 657, 271
 Danforth, C. W., & Shull, J. M. 2005, ApJ, 624, 555 (Paper 1)
 Danforth, C. W., Shull, J. M., Rosenberg, J. L., & Stocke, J. T. 2006, ApJ, 640, 205 (Paper 2)
 Davé, R., et al. 1999, ApJ, 511, 521
 Davé, R., et al. 2001, ApJ, 552, 473
 Ellison, S. L., Songaila, A., Schaye, J., & Pettini, M. 2000, AJ, 120, 1175
 Fang, T., Marshall, H. L., Lee, J. C., Davis, D. S., & Canizares, C. R. 2002, ApJ, 572, L127
 Fang, T., Canizares, C. R., & Yao, Y. 2007, ApJ, 670, 992

- Fardal, M. A., Giroux, M. L., & Shull, J. M. 1998, *AJ*, 115, 2206
- Fechner, C., et al. 2006, *A&A*, 455, 91
- Gehrels, N. 1986, *ApJ*, 303, 336
- Gibson, B. K., Giroux, M. L., Penton, S. V., Putman, M. E., Stocke, J. T., & Shull, J. M. 2000, *AJ*, 120, 1830
- Gibson, B. K., Giroux, M. L., Penton, S. V., Stocke, J. T., Shull, J. M., & Tumlinson, J. 2001, *AJ*, 122, 3280
- Giroux, M. A., & Shull, J. M. 1997, *AJ*, 113, 1505
- Gnat, O., & Sternberg, A. 2007, *ApJS*, 168, 213
- Haardt, F., & Madau, P. 1996, *ApJ*, 461, 20
- Haardt, F., & Madau, P. 2001, in *Clusters of Galaxies and the High Redshift Universe Observed in X-rays*, Neumann, D. M., Tran, J. T. V., 64
- Indebetouw, R., & Shull, J. M. 2004, *ApJ*, 607, 309
- Kaastra, J., Werner, N., den Herder, J. W., Paerels, F., de Plaa, J., Rasmussen, A. P., & de Vries, C. 2006, *ApJ*, 652, 189
- Kim, T.-S., Cristiani, S., & D'Odorico, S. 2002, *A&A*, 383, 747
- Lehner, N., Savage, B. D., Richter, P., Sembach, K. R., Tripp, T. M., & Wakker, B. P. 2007, *ApJ*, 658, 680
- McWilliam, A. 1997, *ARA&A*, 35, 503
- Moos, H. W., et al. 2000, *ApJ*, 538, L1
- Morton, D. C. 2003, *ApJS*, 149, 205
- Nicastro, F., et al. 2005, *ApJ*, 629, 700
- Peimbert, M., Luridiana, V., & Peimbert, A. 2007, *ApJ*, 666, 636
- Penton, S. V., Stocke, J. T., & Shull, J. M. 2000, *ApJS*, 130, 121
- Penton, S. V., Shull, J. M., & Stocke, J. T. 2000, *ApJ*, 544, 150
- Penton, S. V., Stocke, J. T., & Shull, J. M. 2004, *ApJS*, 152, 29
- Pettini, M., Madau, P., Bolte, M., Prochaska, J. X., Ellison, S. L., & Fan, X. 2003, *ApJ*, 594, 695
- Prochaska, J. X., Weiner, B. J., Chen, H.-W., & Mulchaey, J. S. 2006, *ApJ*, 643, 680
- Rajan, N., & Shull, J. M. 2008, in preparation
- Rasmussen, A. P., Kahn, S. M., Paerels, F., den Herder, J. W., Kastra, J., & de Vries, C. 2007, *ApJ*, 656, 129
- Richter, P., Savage, B. D., Tripp, T. M., & Sembach, K. R. 2004, *ApJS*, 153, 165
- Sahnow, D. J., et al. 2000, *ApJ*, 538, L7
- Salucci, P., & Persic, M. 1999, *MNRAS*, 309, 923
- Savage, B. D., Sembach, K. R., Tripp, T. M., & Richter, P. 2002, *ApJ*, 564, 631
- Sembach, K. R., Wakker, B. P., Savage, B. D., Richter, P., Meade, M., Shull, J. M., Jenkins, E. B., Sonneborn, G., & Moos, H. W. 2003, *ApJS*, 146, 165
- Sembach, K. R., & Savage, B. D. 1992, *ApJS*, 83, 147
- Sembach, K. R., & Savage, B. D. 1994, *ApJ*, 431, 201
- Sembach, K. R., Savage, B. D., Lu, L., & Murphy, E. M. 1999, *ApJ*, 515, 108
- Scannapieco, E., et al. 2006, *MNRAS*, 365, 615
- Schaye, J. 2001, *ApJ*, 559, 507
- Shull, J. M., Roberts, D., Giroux, M., Penton, S., & Fardal, M. 1999, *ApJ*, 600, 570
- Shull, J. M., et al. 2000, *ApJ*, 538, L13
- Shull, J. M. 2003, in *The IGM/Galaxy Connection: The Distribution of Baryons at $z = 0$* , ed. J. Rosenberg, M. Putman, *ASSL*, Vol. 281, 231
- Shull, J. M., et al. 2004, *ApJ*, 600, 570
- Songaila, A. 1997, *ApJ*, 490, L1
- Songaila, A. 1998, *AJ*, 115, 2184
- Songaila, A. 2001, *ApJ*, 561, L153
- Spergel, D. N., et al. 2007, *ApJS*, 170, 377
- Stocke, J. T., Shull, J. M., & Penton, S. V. 2006a, in *Planets to Cosmology: Essential Science in the Final Years of the Hubble Space Telescope*, *STScI Symposium Series*, Vol. 18, 111
- Stocke, J. T., Penton, S. V., Danforth, C. W., Shull, J. M., Tumlinson, J., & McLin, K. M. 2006b, *ApJ*, 641, 217
- Sutherland, R. S., & Dopita, M. A. 1993, *ApJS*, 88, 253
- Telfer, R. C., Kriss, G. A., Zheng, W., Davidsen, A. F. & Tytler, D. 2002, *ApJ*, 565, 773
- Tripp, T. M., Savage, B. D., & Jenkins, E. B. 2000, *ApJ*, 534, L1
- Tripp, T. M., et al. 2004, in *Astrophysics in the Far Ultraviolet: Five Years of Discovery with FUSE*, *AIP Conf. Ser.*, Vol. 348, 349
- Tripp, T. M., et al. 2008, *ApJ*, in press, (arXiv:0706.1214)
- Tumlinson, J., & Fang, T. 2005, *ApJ*, 623, L97
- Weymann, R. J., Vogel, S. N., Veilleux, S. & Eps, H. W. 201, *ApJ*, 561, 559
- Westbrook, J., Shull, J. M., Danforth, C. W., & Collins, J. 2008, in preparation